Arabian Journal of Chemistry (2022) **15**, 103510

King Saud University

Arabian Journal of Chemistry

www.ksu.edu.sa
www.sciencedirect.com

ORIGINAL ARTICLE

Synthesis and computational study of 4-hydroxylbenzamide analogous as potential anti-breast cancer agent

Chia Hui Low [a], **Habsah Mohamad** [a,*], **Siti Fatimah Zaharah Mustafa** [a], **Khamsah Suryati Mohd** [b], **Nor Elani Mat Nafi** [b]

[a] *Institute of Marine Biotechnology, Universiti Malaysia Terengganu, 21030 Kuala Nerus, Terengganu, Malaysia*
[b] *School of Agriculture Sciences and Biotechnology, Faculty of Bioresources and Food Industry, Universiti Sultan Zainal Abidin, Besut Campus, 22200 Besut, Terengganu, Malaysia*

Received 29 July 2021; accepted 14 October 2021
Available online 25 October 2021

KEYWORDS

Benzamide analogues;
Histone deacetylase II (HDAC II) enzymes;
Janus kinase (JAK2) enzymes;
Epidermal growth factor receptor (EGFR);
Cytotoxic

Abstract Due to their role in cell growth and survival, HDAC (II), JAK 2 and EGFR receptors are important targets in many chemotherapies that aim to produce their biological response in malignancy solid tumors. In this work, several 4-hydroxybenzamide analogues coupled with 1,3-benzodioxole, a,ß-unsaturated carbonyl, and *tert*-butyl ester bases small molecules were synthesized via imidation, EDC coupling, and etherification reactions, then bio-active 4-hydroxybenzamide analogues were studied using quantum calculations and molecular docking. The Frontier molecular orbitals and energy gap values were calculated using Time-Dependent Density Functional Theory (TD-DFT). Docking results showed A and E as potent JAK2 inhibitors. B, C, and F may be good HDAC II inhibitors. D may act as a potent EGFR inhibitor. These were followed by cytotoxic evaluation of 4-hydroxybenzamide analogues on human estrogen receptor breast cancer cells (MCF-7), metastatic breast adenocarcinome cancer cells (MDA-MB-231), and fibroblast cells (NIH/3T3) respectively. Molecule E was found to have insignificant apoptosis against MCF 7 cell line and MDM-MD-231 cell lines with IC50 value 5.0 μg⁄mL and 5.0 μg⁄mL respectively.

1. Introduction

The most commonly diagnosed cancer among females all over the world today is breast cancer (Feng et al., 2018). According to American Cancer Society (2021), breast cancer occurs in roughly more than 28,150 US women. After increased public awareness, breast cancer death rate has continued to decrease due to earlier detection, with the figure declining 41% from 1989 to 2018, representing 403,200 prevented breast cancer

* Corresponding author at: Institute of Marine Biotechnology, Universiti Malaysia Terengganu, 21030 Kuala Nerus, Terengganu, Malaysia.
E-mail address: habsah@umt.edu.my (H. Mohamad).
Peer review under responsibility of King Saud University.

Production and hosting by Elsevier

https://doi.org/10.1016/j.arabjc.2021.103510

deaths. Causes of breast cancer include tobacco products, obesity, lifestyle, aging, genetic predispositions and not breastfeeding (Feng et al., 2018; Elkum et al., 2014). Despite the reduced statistic; unfortunately, breast cancer still remains the second leading cause of death among females in the world.

The most common types of breast cancer are estrogen receptor (MCF-7) and triple negative breast cancer (MDM-MD-231) (Feng et al., 2018; Elkum et al., 2014). Between the two, triple negative breast cancer (MDM-MD-231) has the most aggressive metathesis behaviour, is invasive, and has limited treatments options (Wang et al., 2018). This is due to its lack of expression status such as estrogen receptor, progesterone receptor, and human epidermal growth factor receptor (Britschgi et al., 2013). One method of breast cancer treatment is chemotherapy. In the current study, key biomolecule targets for chemotherapy were Histone Deacetylase 2 (HDAC 2), Janus kinase 2 (JAK2), and Epidermal growth factor receptor (EGFR) (Singh and Bast, 2014; Lin et al., 2018; Yelton and Ray, 2018). JAK2 receptor's signalling pathway plays a crucial role in the progression, invasion, and metathesis of breast cancer (Britschgi et al., 2013; Lin et al., 2018; Jia et al., 2016; Tian et al., 2020). HDAC II's and EGFR's signalling mutations play a crucial rule in the development of solid tumours such as breast cancer, colon cancer, lung cancer, prostate cancer, and cervical carcinoma (Singh and Bast, 2014; Siegelin and Borczuk, 2014).

To date, structural modifications on benzamide bases have been extensively studied to enhance the effectiveness of drugs, such as anti-tumour agents as well as cholesterol lowering agents and anti-bacterial agents (Nikolic et al., 2011; Staels and Fruchart, 2005; Stec et al., 2012). This is because carbonyl amide (CONH) functionalities are key structural motifs in active pharmacology ingredients (API) (Staels and Fruchart, 2005; Stec et al., 2012; Liew et al., 2019). Moreover, carbonyl amide functionalities are capable of interacting with various biological targets through hydrogen bonding (Liew et al., 2019). In the current study, several bio-active fragments such as 1,3-benzodioxole, a,ß-unsaturated carbonyl, and alkyl-ester (Figure 1) were chosen to be coupled to 4-hydroxybenzamide structure due to their ability to inhibit HDAC (ii) and JAK2 receptors, which can slow down proliferation of cancer cell (Ediriweera et al., 2019; Abu Bakar et al., 2018; Kumar et al., 2018; Piekna-Przybylska et al., 2016; Eckschlager et al., 2017). Besides, these bio-active fragments and their derivatives have displayed a wide range of biological activities such as anti-inflammatory, anti-plasmodial, and Alzheimer's disease (Ur Rashid et al., 2019; Gonring-Salarini et al., 2019; Szczepańska et al., 2018).

In this study, benzamide derivatives were synthesized by adding the 1,3-benzodioxole, tertbutyl ester, and a,ß-unsaturated carbonyl moiety, with the aim to improve their cytotoxic activity against breast cancer cells (MCF-7 and MDM-MD-231). The chemical reactivity parameters and electronic properties of the selective molecules were predicted by quantum calculations such as density functional theory and time dependence-density functional theory. Molecular docking studies of synthesized compounds on histone deacetylase II (HDAC II), Janus tyrosine kinase (II), and Epidermal growth factor receptor (EGFR) were carried out to identify the key pharmacology interactions. Finally, the cytotoxicity assay studies of synthesized compounds against MCF cell lines, MDA-MD-231 cell lines, and NIH/3T3 cell lines were conducted.

2. Material and methods

2.1. Synthesis of benzamides derivatives

2.1.1. *Synthesis of N-cinnamoyl-4-hydroxybenzamide (A)*

Hydroxy-benzamide (2.66 mmol, 3.64 g) and cinnamoyl chloride (2.66 mmol, 4.42 g) in 40 mL anhydrous pyridine was added into 50 mL two-neck round-bottom flask with appropriate magnetic stirrer at reflux condition under nitrogen gas flow. The progress of reaction was monitored by Thin Layer Chromatography (TLC) (Hexane: ethyl acetate; 1:1). Finally, the solvent was removed and the purification by column chromatography (ethyl acetate: hexane; 1:9) afforded *N*-cinnamoyl-4-hydroxybenzamide (0.43 g, 6%). Data analysis: ^{1}H NMR (CH_3OD, 400 MHz): δ 6.67 (1H, d, J = 16 Hz, H-6), 7.82 (1H, d, J = 16.04, H-5), 7.30–7.61 (5H, m, H-8, H-9, H-10, H-11, H-12), 7.72 (2H, d, J = 8.68, H-1, H-13), 7.31 (2H, d, J = 8.68, H-2, H-14). ^{13}C NMR (CH_3OD, 100 MHz): δ 164.6 (CONH, C-4, C-4*), 154.4 (C-OH, C-15), 147.5 (C = CH, C-6), 109.3 (C = CH, C-5), 128.8 (2CH, C-1,C-13), 128.5 (2CH, C-11, C-9), 133.5 (2CH, C-12,C-8), 122.8 (2CH, C-2, C-14), 134.0 (CH, C-7), 116.0(C, C-10), 117.9 (C, C-3). ATR-IR (cm^{-1}) : v (O-H) 3392 cm^{-1}, v (N-H) 3170, v (C = O) 1729.07, C = $C_{benzene}$ 1655–1632, v (C-N) 1210–1336, v (C-O) 1000–1017. UV–vis (MEOH) λ (nm): (n → π*) 283.50_{max}, (π → π*)223.5, (π → π*)218.5. HRMS (positive mode) m/z calculated for $[C_{16}H_{13}NO_3]^+$: 267.0895, $[M + H]^+$; found: 268.0968 (see Scheme 1).

2.1.2. *Synthesis of N-(4-hydroxylbenzoyl)-1,3-benzodioxole-5-carboxamide (B)*

4-Hydroxybenzamide (1.96 mmol, 2.68 g) and 1,3-benzodioxo chloride (1.96 mmol, 3.60 g) in 40 mL anhydrous pyridine was put into 50 mL two-neck flask with appropriate magnetic stirrer at refluxed condition under nitrogen gas flow. The progress of reaction was monitored by TLC (Hexane: ethyl acetate; 1:1). Finally, the solvent was removed, and the purification by column chromatography (ethyl acetate: hexane; 1:9) afforded *N*-(4-hydroxylbenzoyl)-1,3-benzodioxole-5-carboxa

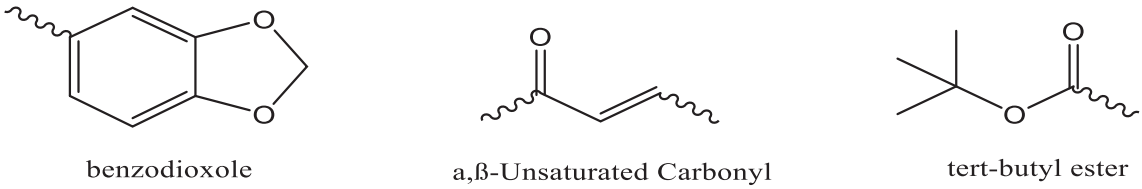

Fig. 1 Chemical structure of bioactive moiety report as cancer properties.

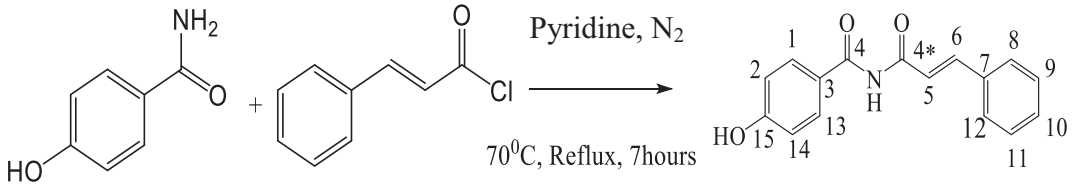

Scheme 1 Synthesis of N-(4-hydroxybenzoyl)-cinnamoylimide derivative) (A).

mide (B) (0.17 g, 3%). Data analysis: ^{1}H NMR (400 MHz, $CDCl_3$): δ 6.10 (2H, s, H-9), 6.92 (1H, d, J = 8.4 Hz, H-11), 7.73(2H, d, J = 8.80 Hz, H-1, H-14), 7.35 (2H, d, J = 8.80 Hz), 7.58 (1H, s, H-7), 7.82 (1H, d, J = 8.00 Hz, H-12). ^{13}C NMR (100 MHz, $CDCl_3$): δ 163.7 (CONHCO, C-4, C-5), 154.3 (C-OH, C-15), 102.2(CH_2, C-9), 154.3(C-O, C-10), 152.7(C-O, C-8), 133.7(2CH, C-2, C-13), 122.9 (2CH, C-1, C-14), 122.4 (C, C-3), 126.6 (CH, C-12), 108.3 (CH, C-11), 118.4(CH, C-6), 154.3(CH, C-10), 148.1 (C, C-8), 109.9 (CH, C-7). ATR-IR v (cm^{-1}): (O-H) 3404.3 cm^{-1}, (N-H) 3182.3 cm^{-1}, (C = O) 1748.2 cm^{-1}, (C = $C_{Benzene}$) 1636.2 cm^{-1}, (C-N) 1393 cm^{-1}-1092 cm^{-1}, (C-O) 1203 cm^{-1}-1040 cm^{-1}. UV–Vis (MeOH) λ (nm): ($\pi \rightarrow \pi^*$) 226.5nm_{max}, ($n \rightarrow \pi^*$) 269.00 nm, ($n \rightarrow \pi^*$) 303.0 nm. HRMS (positive mode) m/z calculated for $[C_{15}H_{11}NO_5]^+$: 285.2550, $[M + Na]^+$; $[M + K]^+$; found: 308.2949; 324.2592 (see Scheme 2).

2.1.3. Synthesis of N-(2-(benzo[d] (Feng et al., 2018; Wang et al., 2018) dioxol-5-yl)ethyl)-4-hydroxybenzamide (C)

4-Hydroxybenzoyl acid (0.36 mmol, 0.50 g) and 2-(1,3-benzodioxo)-ethyl-1-amine (0.36 mmol, 0.53 g) in 40 mL anhydrous aceonitrile was added with acetonitrile (50 mL) in two-neck flask with appropriate magnetic stirrer at reflux condition under nitrogen gas flow. The reaction mixture in the flask was cooled down by adding ice cubes. Meanwhile, equal-molar quantities of 1-ethyl-3-(3-dimethylaminopropyl) carbodiimide (0.36 mmol, 0.69 g) and 0.44 g of 4-dimethylaminopyridine were added to cool mixture. The progress of reaction was monitored by TLC (Hexane: ethyl acetate; 1:1). Finally, the solvent was removed. The purification by column chromatography (ethyl acetate: hexane; 1:9) was done to afford *N*-(2-(benzo[d] dioxol-5-yl)ethyl)-4-hydroxybenzamide (0.72 g, 70%). Data analysis: ^{1}H NMR (400 Hz, acetone d_6): δ 2.81 (2H, t, J = 7.36, H-8), 3.59 (2H, m, H-9), 5.94 (2H, s, H-1), 6.7–6.78 (3H, m, H-4, H-5, H-7), 6.87 (2H, d, J = 8.84, H-14,H-15), 7.66 (NH, br, H-18), 7.77 (2H, d, J = 8.8, H-12, H-13), 9.00 (OH, br, H-17). ^{13}C NMR (100 MHz, acetone d_6) : δ 166.2 (CONH, C-10), 160.1(C-OH, C-16), 147.7 (C-O, C-2), 146.0(C-O, C-3), 114.8 (2CH, C-14, C-15), 41.4(CH_2, C-9), 35.4 (CH_2, C-8), 100.8 (CH_2, C-1), 129.0 (2CH, C-12, C-13), 126.3 (C, C-6), 126.3 (C, C-11), 121.7(CH, C-5), 107.9 (CH, C-4), 109.0 (CH, C-7), and 133.6 (C, C-6). ATR-IR (cm^{-1}): v (N-H), 3120.11, v (O-H), 3414.14, v (C = O), 1632.51, v (C = C)$_{aromatic}$ 1592.86, v (C-N) 1282.38–1311.23, v (C-O), 1035.71–1241.32. UV–Vis (MEOH) λ (nm): ($n \rightarrow \pi^*$) 252.50 $_{max}$. HRMS (positive mode) m/z calculated for $[C_{16}H_{15}NO_4]^+$: 285.1001, $[M + H]^+$;$[M + Na]^+$found: 286.1074; 308.0892 (see Scheme 3).

2.1.4. Synthesis of N-(2-(1,3-benzodioxol-5-yl)ethyl)-1H-indole-2-carboxamide (D)

Indole-2-carboxylic acid (3.10 mmol, 0.50 g) and 1,3-benzodioxo-ethylamine (3.10 mmol, 0.51 g) in 40 mL anhydrous aceonitrile was added with 50 mL aceonitrile in two-neck flask at refluxed condition under nitrogen gas flow. The progress of reaction was monitored by TLC (Hexane: ethyl acetate; 1:1). The reaction mixture in the flask was cooled down by adding ice cubes. Meanwhile, equal- molar quantities of 1-ethyl-3-(3-dimethylaminopropyl)carbodiimide (3.10 mmol, 0.62 g) and 0.10 g of 4-dimethylaminopyridine were added to cool mixture. Finally, the solvent was removed, and the purification using column chromatography was done (Ethyl acetate: hexane; 1:9) to afford *N*-(2-(1,3-benzodioxol-5-yl)ethyl)-1H-indole-2-carboxamide (0.69 g, 70%). ^{1}H NMR (DMSO d_6, 400 MHz): δ 2.78 (2H, t, J = 7.2, H-8), 3.51 (2H, q, J = 6.8, H-9), 5.97 (1H, s, H-1), 6.72(1H, dd, J = 7.6, 1.6 Hz, H-5), 6.82 (1H, d, J = 8.00, H-4), 6.86(1H, s, H-7), 7.40(1H, td, J = 8 Hz,0.8 Hz, H-18), 7.12(1H ,s, H-12), 7.18 (1H, td, J = 8.2, 1.2 Hz, H-17), 7.45 (1H, dd, J = 8.00 Hz, 0.4 Hz, H-16), 7.61(1H, d, J = 8.00 Hz, H-15), 8.53 (N-H, br, H-19), 11.57(CONH, br, H-20). ^{13}C NMR (DMSO d_6, 100 Hz): δ 35.4 (CH_2, C-8), 41.1(CH_2, C-9), 101.1(CH_2, C-1), 145.9(C-O, C-3), 147.6(C-O, C-2), 161.5(CONH, C-10), 136.85(C, C-14), 133.8 (C = C, C-11), 132.3 (C, C-13), 127,6 (C, C-6), 108.6 (CH, C-4), 102.8(CH, C-7), 109.5 (CH, C-15), 112.8 (C = C, C-12), 120.2 (CH, C-18), 121.9 (CH, C-16), 122.1 (CH,C-17), 123.7(CH, C-5). ATR-IR v (cm^{-1}): (N-H) 3286.14 cm^{-1}-3412.83 cm^{-1}, (C = O) 1635.14 cm^{-1}, (C = C)$_{aromatic}$, 1441.12 cm^{-1}-1571.6 cm^{-1}, (C-N) 1312.73 cm^{-1}, (C-O) 1004.11 cm^{-1}-1034.69 cm^{-1}. UV–Vis (MeOH) λ (nm): ($n \rightarrow \pi^*$) 292.50 nm $_{max}$ HRMS (positive

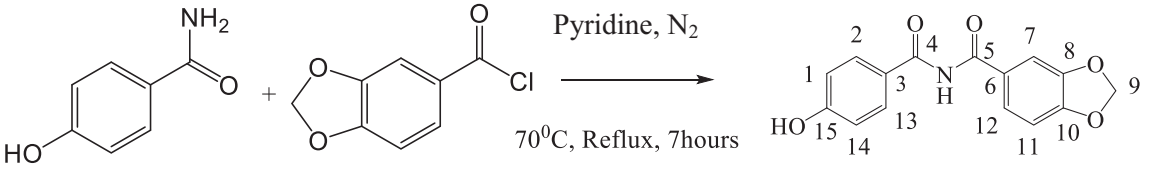

Scheme 2 Synthesis of *N*-(4-hydroxylbenzoyl)-1,3-benzodioxole imide (B).

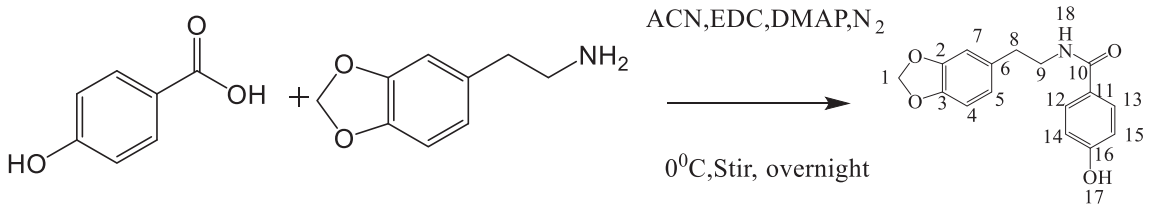

Scheme 3 Synthesis of *N*-(2-(1,3-benzodioxol-5-yl)ethyl-4-hydroxybenzamide.

mode) *m/z* calculated for $[C_{18}H_{16}N_2O_3]^+$: 308.1161, $[M + Na]^+$; [M + H]; $[M + Li]^+$; found: 331. 1056; 309.1233; 315.1314 (see Scheme 4).

2.1.5. Synthesis of N-(4-hydroxyphenethyl)cinnamamide (E)

Currently, synthesis of 4-hydroxylbenzoyl-cinnamoyl via EDC-DMAP method has not been reported. Cimaonyl acid (0.34 mmol, 0.50 g) and tyramine (0.34 mmol, 0.47 g) in 40 mL anhydrous aceonitrile was added with 50 mL aceonitrile in two-neck flask with appropriate magnetic stirrer at cool condition (0 °C) under nitrogen gas flow. Meanwhile, equal-molar quantities of 1-ethyl-3-(3-dimethylaminopropyl)carbodiimide (EDC) (0.34 mmol, 0.65 g) and 0.10 g of 4-dimethylaminopyridine (DMAP) were added to cool mixtures. The progress of reaction was monitored by TLC (hexane: ethyl acetate; 1:1). The reaction mixture in the flask continued to be cooled down by adding ice cubes. Finally, the solvent was removed and the purification by column chromatography was done (ethyl acetate: hexane; 1:9) to afford *N*-(4-hydroxyphenethyl)cinnamamide (E). ^{1}H NMR (CD_3OD, 400 MHz): δ 2.78 (2H, t, J = 7.4 Hz, H-11), 3.49 (2H,t, J = 7.4 Hz, H-10), 6.59 (1H, d, J = 15.76 Hz, H-8), 6.74 (2H, d, J = 8.4, H-15, H-16), 7.07 (2H, d, J = 8.4, H-13, H-14), 7.34–7.56 (6H, m, H-2, H-3, H-4, H-5, H-6, H-7). ^{13}C NMR (CD_3OD, 100 MHz): δ 34.4 (CH_2, C-11), 41.2 (CH_2, C-10), 155.5 (C-OH, C-17), 167.2 (CONH, C-9), 140.3 (C = C, C-7), 120.46 (C = C, C-8), 114.5 (2CH, C-15, C-16), 129.4 (2CH, C-13,C-14), 128.5 (2CH, C-2, C-6), 134.9 (C, C-1), 129.9 (C, C-12), 127.4 (CH, C-4). 129.4(2CH, C-3,C-5). ATR-IR ν (cm^{-1}): (N-H) 3287.86 cm^{-1}, (C = O) 1721.33 cm^{-1}, (C = $C_{aromatic}$) 1459.8 cm^{-1}-1647.65 cm^{-1}, (C-N) 1251.33 cm^{-1} , (C-O) 1018.84 cm^{-1}-1073.17 cm^{-1}. UV–Vis (MeOH) λ (nm): ($n \rightarrow \pi^*$) 280.50nm_{max}, ($\pi \rightarrow \pi^*$) 217 nm. HRMS (positive mode) *m/z* calculated for $[C_{17}H_{17}NO_2]^+$: 267.1259, $[M + H]^+$; $[M + Na]^+$; found: 268.1332; 290.1152 (see Scheme 5).

2.1.6. Synthesis of tert-butyl 2-(4-carbamoylphenoxy)-2-methylpropanoate (F)

Equal molar quantities of 4-hydroxybenzamide (0.36 mmol, 0.50 g), *tert*-butyl-bromoisobutyrate (0.36 mmol, 0.80 g), and K_2CO_3 (0.36 mmol, 0.50 g) were added with dry acetonitrile (50 mL) into two-neck round-bottom flask. The reaction mixture was refluxed for 5 h. After completion of the reaction, potassium carbonate (K_2CO_3) was removed in a sintered funnel, and the filtrate was concentrated under vacuum and subjected to column chromatography (silica gel 100–200 mesh, EtOAc/hexane 3:7) to afford *tert*-butyl 2-(4-carbamoylphenoxy)-2-methylpropanoate (F) (0.91 g, 90%). Data analysis ^{1}H NMR (400 MHz, $CDCl_3$): δ 7.74(2H, d, J = 8.88 Hz, H-3, H-4), 6.84 (2H, d, J = 8.84 Hz, H-5, H-6), 6.28 (NH_2, br), 1.61 (6H,s, H-8, H-8*), 1.42 (9H, s, H-11, H-11*,H-11**,). ^{13}C NMR (100 MHz, $CDCl_3$): δ 25.3 ($2CH_3$,C-8, C-8*), 27.7 ($3CH_3$, C-11, C-11*, C-11**), 79.6 (C-O, C-12), 82.2 (C-O, C-9), 117.5 (2CH, C-5, C-6), 126.0 (C, C-2), 128.9 (2CH C-3, C-4), 158.9 (C-O, C-7), 169.3 ($CONH_2$, C-1), 172.8 (-O-C = O, C-10), 158.9 (C-O, C-7). ATR-IR ν (cm^{-1}): (N-H) 3414.00–3170.97 cm^{-1}, (C = O) 1720.50 cm^{-1}, (C = $C)_{benzene}$ 1458.18 cm^{-1}-1604.77 cm^{-1}, (C-O) 1138.00.6 cm^{-1}-1168.86 cm^{-1}, (C-N) 1303.88-cm^{-1}-1384.89 cm^{-1}. UV–Vis (MEOH) λ (nm): 251 nm_{max}: HRMS (positive mode) *m/z* calculated for $[C_{15}H_{21}NO_4]^+$: 279.3360, $[M + H]^+$; [M + Na]; found: 280.1546; 302.1361 (see Scheme 6).

2.1.7. Synthesis of ethyl 2-(4-carbamoylphenoxy)-2-methylpropanoate (G)

Equal molar quantities of 4-hydroxybenzamide (0.36 mmol, 0.5 g), ethyl-2-bromo-2-methylpropionate (0.36 mmol, 0.71 g), and K_2CO_3 (0.36 mmol, 0.50 g) were added with aceonitrile (50 mL) into two-neck round-bottom flask (50 mL). The reaction mixture was refluxed for 4 h. After completion of the reaction, K_2CO_3 was removed using a sintered funnel, and the filtrate was concentrated under vacuum and subjected to column chromatography (silica gel 100–200 mesh, EtOAc/hexane 3:7) to give pure ethyl 2-(4-carbamoylphenoxy)-2-methylpropanoate as a white precipitate. (0.86 g, 95%). Data analysis: ^{1}H NMR ($CDCl_3$, 400 MHz):δ 7.74 (2H, d, J = 8.84 Hz, H-3, H-4), 6.83 (2H, d, J = 8.8, H-5, H-6), 6.27 (NH_2, br), 4.23 (2H, q, J = 7.13, H-11), 1.64 (6H, s, H-8, H-8*), 1.22 (3H, t, J = 7.14 Hz, H-12). ^{13}C NMR (100 MHz, $CDCl_3$), δ 14.0 (CH_3, C-12), 25.4 ($2CH_3$, C-8, C-

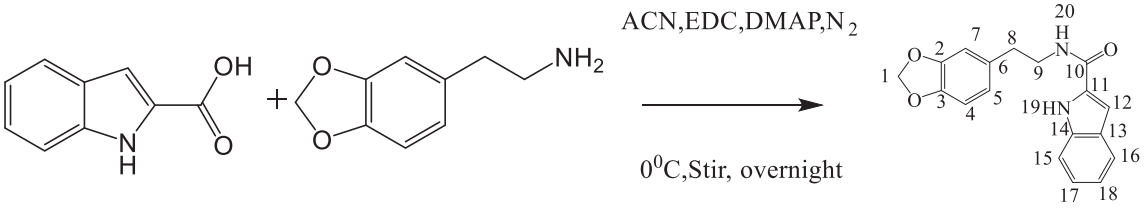

Scheme 4 Synthesis of *N*-(2-(1,3-benzodioxol-5-yl)ethyl)-1H-indole- 2-carboxamide (D).

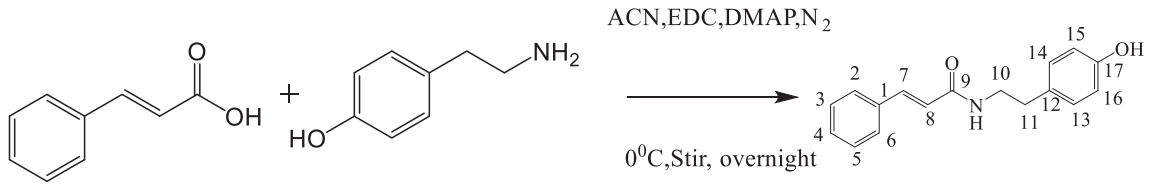

Scheme 5 Synthesis of 4-hydroxylbenzoyl-cinnamoyl amide (E).

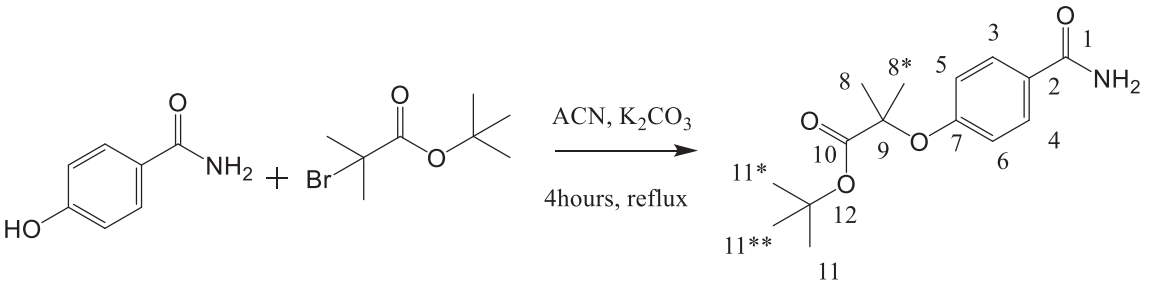

Scheme 6 Synthesis of *tert*-butyl-2-methylpropanoate 4-oxyl-benzamide (F).

8*), 61.7 (CH_2, C-11), 79.3 (C-O, C-9), 117.8 (2CH, C-5, C-6), 126.4 (C,C-2), 129.0 (2CH, C-3,C-4), 158.7 (C-O, C-7), 173.9 (O-C = O, C-10), 169.2 ($CONH_2$, C-1). DEPT 135; positive phase: 25.4 ($2CH_3$, C-8, C-8*), 14.0 (CH_3, C-12), 129.0 (2CH, C-3, C-4), 117.8 (2CH, C-5, C-6), Negative phase: 61.7 (CH_2, C-11). ATR-IR ν (cm^{-1}): (N-H) 3417.86 cm^{-1}-3170.97 cm^{-1}, (C = O) 1720.5 cm^{-1} ,(C = $C_{benzene}$) 1604.77 cm^{-1}-1643.35 cm^{-1}, (C-O) 1141.86 cm^{-1}, (C-N) 1257.59 cm^{-1}-1388.75 cm^{-1}. UV–vis (MEOH) λ(nm): (n → π*) 243.50 nm $_{max}$, (n → π*) 278.50 nm HRMS (positive mode) *m*/*z* calculated for $[C_{13}H_{17}NO_4]^+$: 251.2820, $[M + Na]^+$; $[M + K]^+$; found: 251.2784; 290.2690 (see Scheme 7).

2.1.8. Synthesis of methyl 2-(4-carbamoylphenoxy)-2-methylpropanoate (H)

Equal molar quantities of 4-hydroxybenzamide (0.36 mmol, 0.50 g), methyl-2-bromo-2-methylpropionate (0.36 mmol, 0.66 g), and K_2CO_3 (0.36 mmol, 0.5 g) were added with acetonitrile (50 mL) into two-neck round-bottom flask. The reaction mixture was refluxed for 4 h. After completion of the reaction, K_2CO_3 was removed in a sintered funnel, and the filtrate was concentrated under vacuum and subjected to column chromatography (silica gel 100–200 mesh, EtOAc/hexane 4:6) to give pure methyl 2-(4-carbamoylphenoxy)-2-methylpropanoate as a white precipitate (0.80, 94%). Data analysis: ^{1}H NMR ($CDCl_3$, 400 MHz): δ 7.73 (2H, d, J = 8.8 Hz, H-3, H-4), 6.83 (2H.d, J = 8.8 Hz, H-5,H-6), 6.00 (NH_2, br), 3.76 (3H, s, H-11), 1.64 (6H, s, H-8,H-8*). ^{13}C NMR ($CDCl_3$, 100 MHz): δ 25.36 (2CH3, C-8, C-8*), 52.69(O-CH_3, C-11), 79.30(C-O, C-9), 117.8 (2CH, C-5, C-6), 129.0 (2CH, C-3,C-4), 126.5 (C, C-2), 158.7 (C-O, C-7), 168.9 ($CONH_2$, C-1), 174.4 (O-C = O, C-10). IR-ATR ν (cm^{-1}): (N-H), 3170.97 cm-1–3417 .86 cm^{-1}, (C = O) 1735.93 cm-1, (C = C), 1643.35.cm^{-1}-1604.77 cm^{-1}, (C-N), 1249.87 cm^{-1}-1388.75 cm^{-1}, (C-O) 1141.86 cm^{-1}. UV–vis (MEOH) λ(nm): (n → π*) 251.50nm_{max}. HRMS (positive mode) *m*/*z* calculated for $[C_{12}H_{15}NO_4]^+$: 237.2550, $[M + H]^+$; [M + K]; found: 238.1078; 276.0443 (see Scheme 8).

2.1.9. Synthesis of methyl 2-(2-carbamoylphenoxy)-2-methylpropanoate (I)

A mixture of 2-hydroxy-benzamide (0.36 mmol, 0.5 g), methyl-2-bromopropionate (0.36 mmol, 0.66 g), and K_2CO_3 (0.36 mmol, 0.5 g) was added with acetonitrile (50 mL) into two-neck round-bottom flask. The reaction mixture was refluxed for four hours. After completion of the reaction, K_2CO_3 was removed in a sintered funnel, and the filtrate was concentrated under vacuum and subjected to column chromatography (silica gel 100–200 mesh, EtOAc/hexane 1:9)

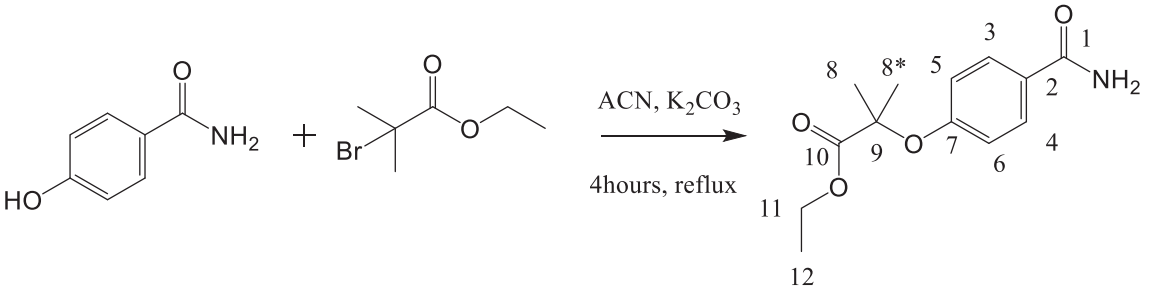

Scheme 7 Synthesis of ethyl-2-methylpropanoate 4-oxyl-benzamide (G).

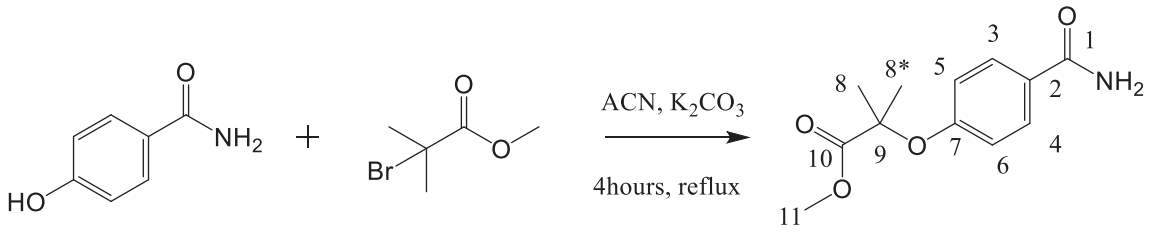

Scheme 8 Synthesis of methyl-2-methylpropanoate 4-oxyl-benzamide (H).

to give pure methyl 2-(2-carbamoylphenoxy)-2-methylpropano ate as a white precipitate (0.68 g, 80%). Data analysis:^{1}H NMR ($CDCl_3$, 400 MHz): δ 1.69 (6H, s, H-8, H-8*), 3.80 (3H, s, H-10), 6.49, 7.91 (2H, br, NH_2), 6.81 (1H, d, J = 8.00 Hz, H-5), 7.29–7.40 (1H, m, H-7), 7.10–7.14 (1H, m, H-6), 8.2–8.17 (1H, dd, H-4). ^{13}C NMR ($CDCl_3$, 100 MHz): δ 25.3 (CH3, C-8, C-8*), 52.9 (O-CH_3, C-11), 81.1 (O-C, C-11), 117.7 (CH, C-5), 122.7 (CH, C-6), 124.4 (C, C-2), 132.5 (CH, C-4),132.6 (CH, C-7), 153.7 (C, C-3), 167.4 ($CONH_2$, C-1), 174.0 (O-C = O, C-9). ATR-IR v (cm^{-1}): (N-H) 3172.9 cm^{-1}-3415.93 cm^{-1}, (C = O) 1716.05 cm^{-1}, (C = C) 1456.26 cm^{-1}-1624.06 cm^{-1}, (C-N) 1265.30 cm^{-1}-1388.75 cm^{-1}, (C-O) 1145.72 cm^{-1}-1022.27 cm^{-1}.UV–vis (MEOH) λ(nm): (n → π*)276mn $_{max}$, (π → π*) 232mn. HRMS (positive mode) m/z calculated for $[C_{12}H_{15}NO_4]^+$: 237.1001 , [M + Li]; [M + Na]; [M + K]; found: 244.2634; 260.0893; 276.0446 (see Scheme 9

2.1.10. Synthesis of methyl 2-(4-formyl-2-methoxyphenoxy)-2-methylpropanoate (J)

Equal molar quantities of 3-methoxyl-4-hydroxybenzaldehyde (0.33 mmol, 0.5 g), methyl-2-bromo-2-methylpropionate (0.33 mmol, 0.73 g), and K_2CO_3 (0.33 mmol, 0.46 g) were added with aceonitrile (50 mL) into two-neck round-bottom flask. The reaction mixture was refluxed for 4 h. After completion of the reaction, K_2CO_3 was removed in a sintered funnel, and the filtrate was concentrated under vacuum and subjected to column chromatography (silica gel 100–200 mesh, EtOAc/hexane 3:7) to give pure methyl 2-(4-formyl-2-methoxyphe noxy)-2-methylpropanoate as a yellowish liquid (0.71 g. 90%). Data analysis: ^{1}H NMR ($CDCl_3$, 400 MHz): δ 1.37 (6H, s, H-10,H-10*), 3.501 (3H, s, H-12), 3.60 (3H, s, H-8), 6.6 (1H, s, H-3), 7.15 (2H, br, H-6, H-7), 9.57 (H-C = O, s). ^{13}C NMR ($CDCl_3$, 100 MHz): δ 24.9 (CH_3, C-10, C-10*), 52.2 (O-CH_3, C-12), 55.44 (O-CH_3, C-8), 80.1 (C-O, C-9), 110.1 (CH, C-3), 117 (CH, C-6), 125.0 (CH, C-7), 131.2 (C, C-2), 150.1 (C-O, C-4), 151.4 (C-O, C-5), 173.6 (O-C = O, C-11), 190.60 (H-C = O, C-1). DEPT 135, Positive phase: 24.86 (CH_3, C-10, C-10*), 52.21 (CH_3, C-12), 88.4 (CH_3, C-8), 110.1 (CH, C-3),117.0 (CH, C-6), 125.0 (CH, C-7), 110.1 (CH, C-3), 117.0 (CH, C-6), 125.03 (CH, C-7). IR-ATR v (cm^{-1}): (CH_3), 3187 cm^{-1}-2895 cm^{-1}, (C = O) 1706.41 cm^{-1} (C = C) 1478 cm^{-1}-1602.09 cm^{-1}, (C-O) 1059.92 cm^{-1}. UV–vis (MEOH) λ (nm): (n → π*) 227 nm $_{max}$, (π → π*) 272 nm, (π → π*) 308 nm. HRMS (positive mode) m/z calculated for $[C_{13}H16O_5]^+$: 252.09977, [M + K]$^+$; found: 291.0839 (see Scheme 10).

2.1.11. Synthesis of tert-butyl 2-(4-formyl-2-methoxyphenoxy)-2-methylpropanoate (K)

Equal molar quantities of the 3-methoxyl-4-hydroxybenzaldehyde (0.33 mmol, 0.50 g), *tert*-butyl-bromo-*iso*-butyrate (0.33 mmol, 0.87 g), and K_2CO_3 (0.33 mmol, 0.46 g) were added with acetonitrile (50 mL) into two-round-bottom flask. The reaction mixture was refluxed for 4 h. After completion of the reaction, K_2CO_3 was removed in a sintered funnel, and the filtrate was concentrated under vacuum and subjected to column chromatography (silica gel 100–200 mesh, EtOAc/hexane 3:7) to give pure *tert*-butyl 2-(4-formyl-2-meth oxyphenoxy)-2-methylpropanoate as a yellowish liquid (0.82 g, 89%). Data analysis: ^{1}H NMR ($CDCl_3$, 400 MHz): δ 1.44 (9H, s, H-13, H-13*, H-13**), 1.66 (6H, s, H-11, H-11*), 3.90 (3H, s, H-8), 6.87 (1H, d, J = 8.4 Hz, H-6), 7.37 (1H,d , J = 8.00, H-4), 7.43 (1H,s, H-5), 9.85 (O = C-H, s, H-2). ^{13}C NMR ($CDCl_3$, 100 MHz): δ 25.2 (2CH_3, C-11, C-11*), 27.7 (3CH_3, C-13, C-13*, C-13**), 56.0 (CH_3, C-8), 80.7(C-O, C-14), 82.1 (C-O, C-10), 172.5 (O-C = O, C-12), 116.5 (CH,C-6), 150.9 (C-O, C-7), 151.2 (C-O, C-9), 130.6 (C, C-3), 125.5 (CH, C-4), 110.0 (CH, C-5), 190.9 (H-C = O, C-1). ATR-IR v (cm^{-1}): (CH_3) 2979.80 cm^{-1}, (C = O) 1721.08 cm^{-1}, (C = C), 1464.7 cm^{-1}-1584 cm^{-1}, (C-O) 1035.60–1121.41 cm^{-1}.UV–vis (MEOH) λ (nm):

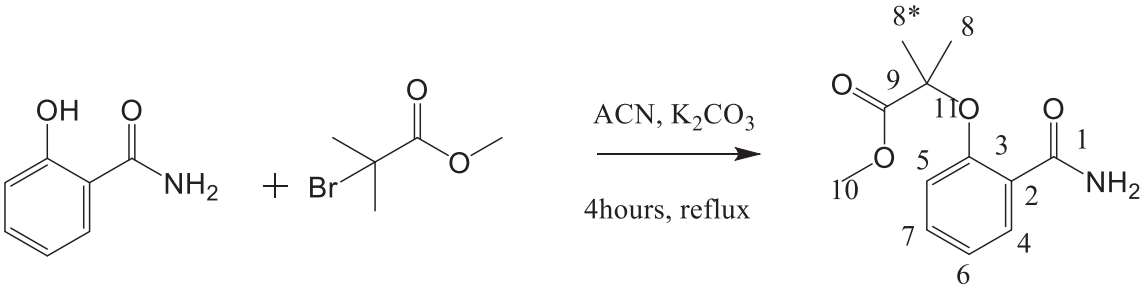

Scheme 9 Synthesis of methyl 2-(2-carbamoylphenoxy)-2-methylpropanoate (I).

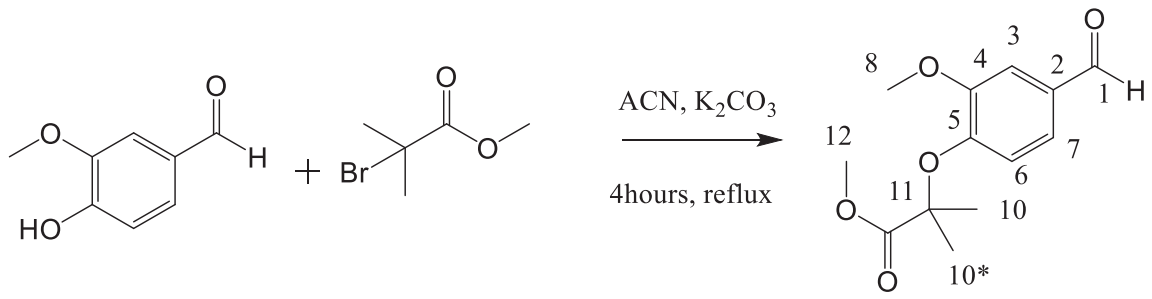

Scheme 10 Synthesis of methyl 2-(4-formyl-2-methoxyphenoxy)-2-methylpropanoate (J).

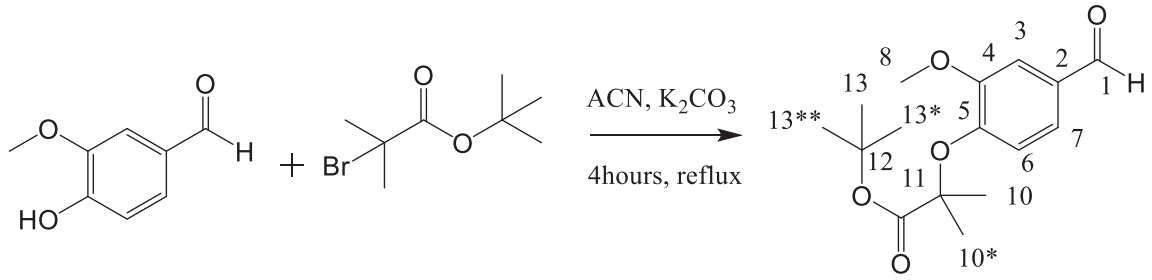

Scheme 11 Synthesis of *tert*-butyl 2-(4-formyl-2-methoxyphenoxy)-2-methylpropanoate(K).

(n → π*) 227.50 nm $_{max}$, (π → π*) 272.50 nm, (π → π*) 308 nm. HRMS (positive mode) *m/z* calculated for $[C_{16}H_{22}O_5]^+$: 294.14672 , $[M + K]^+$; found: 333.1313 (see Scheme 11).

2.2. Ligand preparation by computational approach

Density functional theory (DFT) is a computational quantum modeling approach used to predict the electronic structure and study the interactions involved between the receptors and the ligands. Geometric parameter of the six selected benzamide derivatives were calculated using the Becke3-Lee-Yang-Parr (B3LYP) method with the 6–31G + (d,p) level of theory using Solvation density model (SMD) upon water environment aided by Gaussian 09. Electronic properties of selected ligands have been studied using TD-SCF/DFT/(B3YLP)/6 + 31G + (d,p)/SMD upon methanol solvent.

2.2.1. Chemical reactivity parameter

Density functional theory protocol provides an excellent framework to define a set of known chemical concepts such as ionization potential (I) (Foresman and Frisch, 1996; Lewars, 2003), electron affinity (EA) (Foresman and Frisch, 1996; Lewars, 2003), chemical hardness (η) (Parr and Pearson, 1983; Parr and Yang, 1984), electronegativity (χ) (Parr and Pearson, 1983; Parr and Yang, 1984), and electrophilicity (ω) (Parr et al., 1999). These reactivity descriptors were obtained by means of energy difference calculations from HOMO and LUMO molecular orbital. The chemical hardness, electronegativity, and electrophilicity are defined as:

Ionization energy(I) = $-E_{HOMO}$
Electron affinity (EA) = $-E_{LUMO}$
Chemical potential (μ) = $-ø$ (I + EA)
Electronegativity (χ) = ø (I + EA)
Global hardness (η) = ø (I-EA)
Electrophilicity (ω) = $\mu^2/2\eta$

Δ Energy gap (E) = E(LUMO)-E(HOMO)

2.3. Molecular docking

All the molecular structures were energy minimized by the quantum mechanic method and converted into sybyl mol2 file format which is readable at the AutoDock Tools 1.5.6 (ADT) interface. After energy quantum mechanic calculations, files were submitted to AutoDock Tools 1.5.6 (ADT). AutoDock Tools 1.5.6 (ADT) was used to calculate Gasteiger partial charges after addition of hydrogen atom and setting up the rotatable bonds of the ligand (Kaur et al., 2017). After that; ligand was saved in PDBQT format. Non-polar hydrogen of protein and ligand were merged. Meanwhile, the protein HDAC II (PDB ID:3KRR (1.80 Å)), JAK2 (PDB ID: 3MAX (2.05 Å)) and EGFR crystal structures (PDB ID: 1 M17 (2.60 Å)), were retrieved from RCSB Protein Data Bank (www.rcsb.org.pdb) (http://www.rcsb.org.pdb). Subsequently, three protein and co-crystalized ligand were converted to Protein Data Bank (PDB) file and saved in the PDBQT file format. Autodock Vina 1.5.6 was used to perform docking using the rigid protein structure. Docking grid with a size of 40 Å × 40 Å × 40 Å was used. The center coordinate of the central atom of the co-crystallized inhibitor was used for each docking. All dockings were run using an 8 Intel Dual-Core 3.0-GHz computer cluster. Autodock Vina presented the docking scores as free energy of binding (ΔG). The vina results of protein-interaction could be viewed by Discovery Studio 2020 software.

2.4. Cell viability assay

Cytotoxicity assay was carried out against MDA-MB-231 (ATCC® HTB-26™), MCF-7(ATCC® HTB-22™), NIH/3T3 (ATCC® CRL-1658™) cell line and cultured at the 37 °C, 5%

CO2 and 90% of humidity All cells were cultured using DMEM or RPMI 1640 medium, respectively and supplemented with 10% (v/v) FBS and 100U/mL of penicillin, 100 g/mL of streptomycin. Cytotoxicity effect of 4-hydroxybenzamide analogous was conducted using 3-[4, 5- dimethylthiazol-2-yl]-2,5 diphenyltetrazolium (MTT) assay that followed the report by (Nafi et al., 2016). MCF-7; MDM-MD-231, and NIH/3T3 cell lines were seeded overnight in 96-well plate at $1x10^5$cell/wall and incubated at 37 °C and 5% CO_2 overnight prior to treatment with compounds at various concentrations (0–100 μg/mL). After 72 h of incubation, 20 μL of MTT reagent (5 mg/mL) was added and incubated for another 4 h at 37 °C. Then, the old media were discarded and 100 μL of 100% DMSO was added to dissolve the purple crystals. Absorbances were recorded at 570 nm and referenced at 630 nm using microplate reader (Tecan, Switzerland). The concentration of compound that resulted in 50% growth inhibition (IC50) was determined from a graph of percentage of cell viability against the concentration of the compound. Doxorubicin was used as the positive control. The percentage of inhibition was calculated using the formula below:

$$Cell viability(\%) = [ODsample at 570nm / ODnegative control at 570nm] \times 100\%$$

3. Results and discussion

3.1. Chemical reactivity parameter of molecule in water phase

The Frontier Molecular Orbitals HOMO and LUMO are responsible for the pharmocophore interactions between ligands and targeted enzymes, although HOMO and LUMO are the main orbitals taking part in chemical stability (Rocha et al., 2018). However, in quantum pharmacology cases, enzymes complex was unnecessarily stabilized by HOMO and LUMO orbital of ligand. Enzymes may be stabilized by other occupied molecular orbital (HOMO-n) and unoccupied molecular orbital (LUMO + n).The values of reactivity parameters calculated for each of the ligand were estimated using the ionization (I), electron affinity (EA), chemical potential (μ), Chemical hardness (η), electronegativity (χ), Global hardness (η) electrophilicity index (ω) and Energy gap (E) are given in Table 1.These parameters play important roles in explaining the charge transfer interaction of ligands with binding site of JAK2, HDAC, and EGFR enzymes. In this study, the energy gap of each A,B, C, D, E, and F were predicted. The energy gap (HOMO-LUMO) of compound decreased as follows: F(5.25237 eV) > C(4.9351 eV) > D(4.5348ev) > E(4.35226 eV) > A(4.1475 eV) > B(4.1157 eV). Theoretically, the order of reactivity increase conforms with the decreases in energy gap (E) values (Jordaan et al., 2020). Oppositely, broad energy gap (E) of the molecules negatively influenced the electron transition from HOMO to LUMO, which subsequently led to a weak affinity of the molecules for receptor (Jordaan et al., 2020). However, the stereoelectronic structures also play crucial roles in bioactivity. This is because receptor requires interaction with correct orientation of ligand to produce its biological response in the cells.

Upon hydration, the chemical potential of each ligand varies from −3.4344 eV to −4.4796 eV. The chemical potential indicated negative values for all molecule, which implies good stability and formation of stable complex with protein. Meanwhile, the electrophilicity index was obtained from means of energy difference calculations from HOMO and LUMO. The electrophilicity index decreased as follows: A (4.8382) > B(4.1181) > E(3.6499) > F(2.9886) > D(2.9243) > C(2.3898). Theoretically, C molecule was suggested to be a better electron donor whereas A acts as better electron acceptor.

3.1.1. Molecular orbital contribution analysis in UV–Vis spectrum

In quantum pharmacology case, ligand A with oscillator force was 0.0834 at a wavelength 328.05 nm with quantum jump of 5.9711 eV (HOMO-1 and LUMO; orbitals, 71.99%). Molecular orbital diagrams showed that second occupied orbital (HOMO-1) of A was located over hydroxyl group and benzene ring with a small part extended over N and O of imide group, whereas lowest unoccupied orbital (LUMO) was distributed largely on cinamoyl group. Next, electronic transition (HOMO-3 → LUMO; 80.35%) of E with higher oscilator force 0.0125 at a wavelength 272.32 nm with the energy gap of 5.3079 eV. For E, the HOMO-3 and LUMO were distributed over hydroxyphenylethyl and cinnamide moiety for protein–ligand complexation.

For 1,3-bezodioxole derivatives (B, C, and D), the HOMO orbital was distributed largely around 1,3-benzodioxol moiety, whereas LUMO was strictly restricted over 4-hydroxyl group and benzamide group (B, C) and indole-benzamide moiety (D). For B, electronic quantum jump was between (HOMO-1 and LUMO; 83.00%) with higher oscillator force 0.0820at a wavelength 302.76 nm with energy gap of 4.6526ev. For C, the higher oscillator force was 0.1329 at 253.60 nm, and showed quantum jump between (HOMO + 1 → LUMO-1, 53.30%) with energy jump 5.8556 eV. For D, the oscillator force was 0.0057 at a wavelength 299.50 nm, and showed energy level with (HOMO → LUMO, 62.58%) 4.5468 eV.

Table 1 Selected chemical reactivity parameters of the A B C D,E, and F determined at the DFT (B3LYP)/6–31 + G(d,p) level of theory upon water phase using SMD model with energy differences approximations.

	Molecular Orbital		EA(ev)	I (ev)	ηa (eV)	χ = −μa (eV)	ω (eV)	E gap (eV)
	Fill-orbital	Empty orbital						
A	HOMO	LUMO	2.4058	6.5533	2.0738	4.4796	4.8382	4.1475
B	HOMO	LUMO	2.0594	6.1751	2.0579	4.1173	4.1188	4.1157
C	HOMO	LUMO	0.9668	5.9019	2.4678	3.4344	2.3898	4.9351
D	HOMO	LUMO	1.3742	5.9090	2.2674	3.6416	2.9243	4.5348
E	HOMO	LUMO	1.8068	6.1590	2.1761	3.9829	3.6449	4.3522
F	HOMO	LUMO	1.3358	6.5881	2.6262	3.9620	2.9886	5.2523

Table 2 Main assignment of the electronic bands of UV–VIS Spectrum, energy, strength of oscillator and wavelength calculated using TD-SCF/DFT (B3LYP)/6-31G + (d,p)/SMD basic set.

Electronic composition contribution	Energy (ev) level		Energy gaps (ev)	Energy (eV) E = hc/λ (theoretical)	Strength of oscillator (f)	Wavelength (nm) (theory)	Wavelength (nm) (experimental)	Type of transitions	Relative deviation (%)	Solvent
A	HOMO-n	LUMO + n								
HOMO-1 → LUMO (71.99%)	−6.6252	−2.3971	5.9711	3.7794	0.0834	328.05	283.50	n → π*	15.71	methanol
HOMO-4 → LUMO (73.94%)	−7.6772	−2.3971	7.0232	4.1504	0.0518	298.73		n → π*	5.37	
B										
HOMO-1 → LUMO (83.00%)	−6.7062	−2.0536	4.6526	4.0591	0.0820	302.76	303.00	n → π*	0.08	methanol
HOMO-4 → LUMO (7.75%)	−7.7346	−2.0536	5.6810	4.2779	0.0777	289.82		n → π*	4.35	
C										
HOMO → LUMO (97.75%)	−5.9062	−0.9625	4.9437	4.7235	0.1131	262.48	252.50	n → π*	3.95	methanol
HOMO-1 → LUMO + 1 (53.3%)	−6.4494	−0.5938	5.8556	4.8890	0.1329	253.60		n → π*	0.44	
D										
HOMO → LUMO (62.58%)	−5.9155	−1.3687	4.5468	4.1397	0.0057	299.50	292.50	n → π*	2.39	methanol
HOMO → LUMO + 1 (35.75%)	−5.9155	−0.4784	5.4371	4.1397	0.0057	299.50		n → π*	2.39	
E										
HOMO-1 → LUMO (95.07%)	−6.4434	−1.8068	4.6366	4.2532	0.6377	291.51	280.50	n → π*	3.93	methanol
HOMO-3 → LUMO (80.35%)	−7.1147	−1.8068	5.3079	4.5529	0.0125	272.32		π → π*	2.92	
F										
HOMO → LUMO (93.65%)	−6.5114	−1.3279	5.1835	4.7445	0.4686	261.32	251.00	n → π*	4.11	methanol
HOMO-1 → LUMO (49.50%)	−7.2546	−1.3279	5.9267	4.8751	0.0076	254.32		n → π*	1.32	

Relative deviation = |(Theoretical/experimental)*100-100.

Lastly, energy gap (HOMO → LUMO; 93.65%) of F with higher oscillator force was 0.4686 at a wavelength 261.32 nm with energy gap of 5.1835ev. Its HOMO orbital was mostly localized on phenyl ring around oxyl benzamide group with a small part distributed over methyl propanoate, whereas LUMO was mainly confined over only oxyl benzamide. HOMO and LUMO orbitals of E mainly take part in enzymes interaction. All these electron transitions between (HOMO-n → LUMO + n) above mainly correspond to the n → π*. LUMO/LUMO + 1 are electron pair acceptor in protein–ligand interaction whereas HOMO/ HOMO-1 are electron pair donor. The UV–Vis spectra obtained from TD-SCF/DFT/B3LYPG(d,p) + /SMD calculations showed agreement with experimental UV–Vis spectrum, where the graph wavelength showed similar value in molecular orbital. The experimental UV–Vis spectrum showed absorption band at 283.50 nm for A, B (303.00 nm), C (252.50 nm), D (292.50 nm), E (280.50 nm) and F (251.00 nm). The molecular orbital contribution analysis and molecular orbitals plot are shown in Table 2 and Table 3 respectively.

3.2. Electrostatic potential surface (EPS)

The electrostatic potential surface maps were adequate for analyzing the possible active sites of the ligand, which is useful for quantum pharmacology modeling. (Rocha et al., 2018) The unequal sharing of electrons distribution, where it can be seen that the red region of CONH end has more electron density than that of the O-H end of the blue region, indicated a characteristic of polar molecules. In water phase, molecule B showed higher electron potential value, from most negative value −9.992e-2 to most positive value 9.992e-2, followed by A, D, C, D, E, and F. This is because molecule B has more electronegativity oxygen atoms when compared to other molecules. The electrostatic potential map of molecules are shown in Fig. 2.

3.3. Molecular docking

3.3.1. Molecular docking analysis of JAK 2 pocket

JAK2-STAT5 (Signal transducers and activators of transcription) is part of the JAK2 enzyme and is activated by cytokines (Tian et al., 2020). It plays important roles in cell proliferation, neural progression, and differentiation (Lin et al., 2018). Overexpression of JAK2-STAT5 signalling pathway can lead to various diseases, such as breast cancer, as well as inflammation and autoimmuse diseases (Nikolic et al., 2011). In this study, the binding energy value of JAK2 was: −7.70Kcal/mol for *N*-cinnamoyl-4-hydroxybenzamide (A) and −7.2Kcal/mol for *N*-(4-hydroxyphenethyl)cinnamamide (E). The hydroxyl (O-H) of A (17O-18H) formed two hydrogen bonds with the key residue LEU932 and GLU 930 ($17O\cdots H\text{-}N_{LEU932}$, bond length = 2.03 Å; $18H\cdots O_{Glu930}$) which are located within a region that has less electrostatic potential. A also formed

Table 3 Main assingment of molecular orbital in UV–Vis spectrum calculated by TD/SCF/DFT B3LYP/6 + 31G + (d,p)/SMD approach for molecules A,B,C,D,E, and F

Molecules	HOMO orbital/HOMO-n orbital	LUMO orbital/LUMO+n orbital	Δ Energy gap (eV)
A (i)	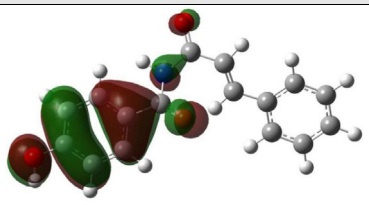 n=1	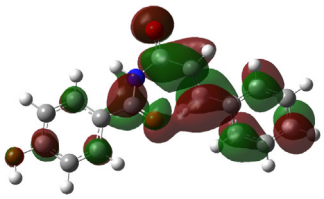 n=0	5.9711
(ii)	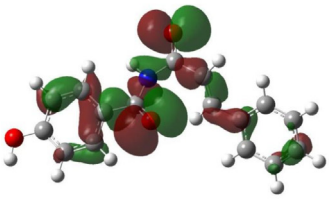 n=4	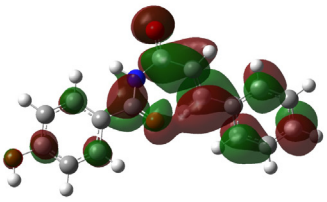 n=0	7.0232
B (i)	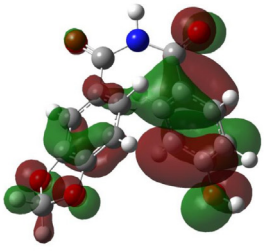 n=-1	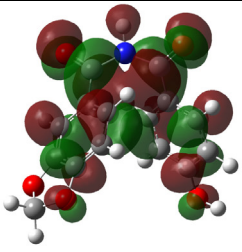 **n=0**	4.6526
(ii)	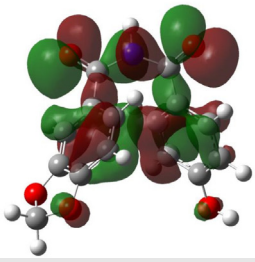 n=4	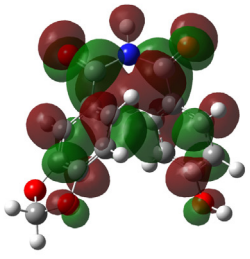 n=0	5.6810
C (i)	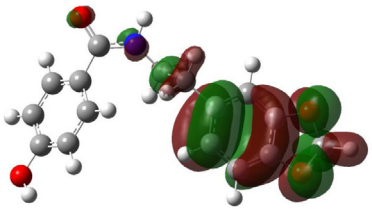 n=0	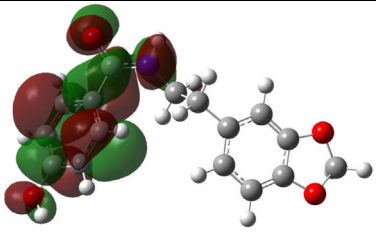 n=0	4.9437
(ii)	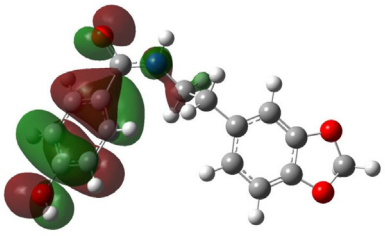 n=1	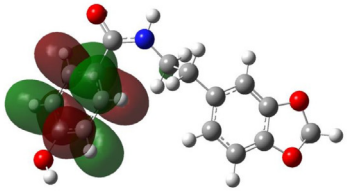 n=1	5.8556

(*continued on next page*)

Table 3 (*continued*)

D (i)	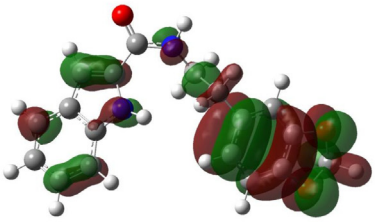 n=0	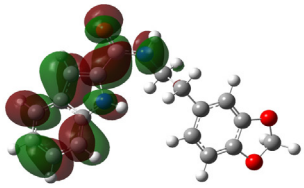 n=0	4.5468
(ii)	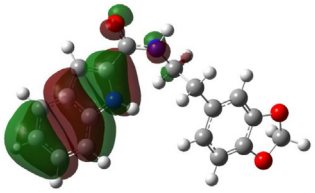 n=1	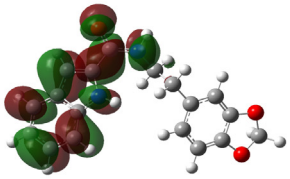 n=0	5.4371
E (i)	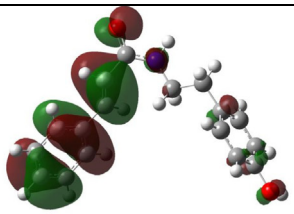 n=1	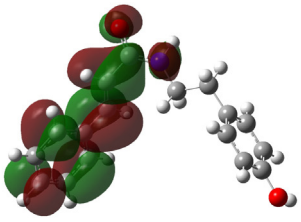 n=0	4.6366
(ii)	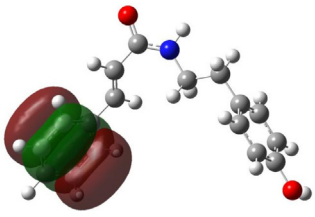 n=3	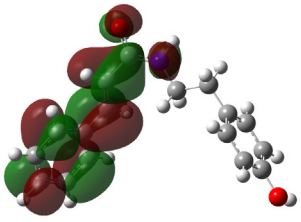 n=0	4.5529
F (i)	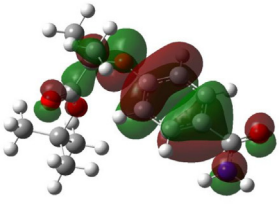 n=0	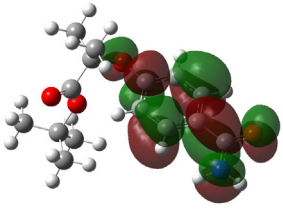 n=0	5.1835
(ii)	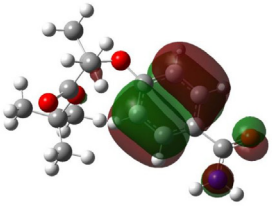 n=1	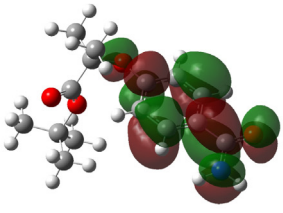 n=0	5.9267

hydrophobic interactions with four key residues: LEU855, LEU 983, ALA880 and VAL 863. Meanwhile, the amide group of E (18 N-19H) formed a hydrogen bond to the carboxylate group ion (COO^-) of residue ASP 994 (19H-O, bond length = 2.37 Å) in the JAK2 pocket. Enzyme structure was stabilized by hydrophobic interactions formed by key residues LEU855, LEU983, ALA880 and others. Ligand interaction diagram of A and with active site of Janus kinase (II) is shown in Fig. 3. Ligand docking analysis of Janus Kinase II enzymes for compound A and E are given in Table 4.

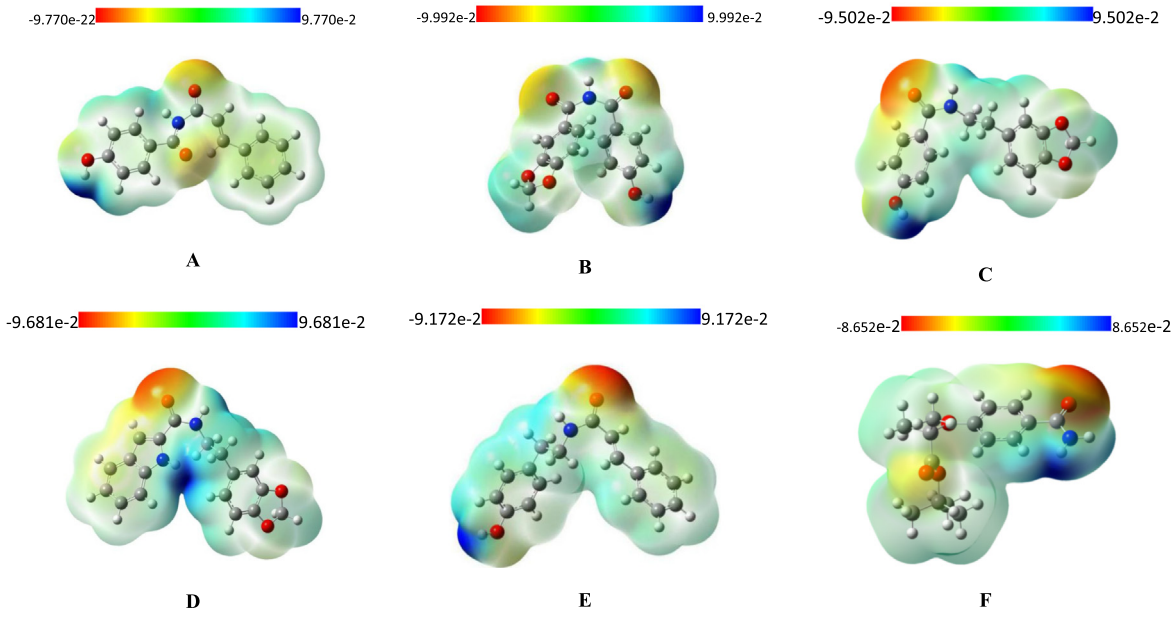

Fig. 2 Electronstatic potential map for ligands A, B,C,D,E and F in water phase. Calculated at DFT (B3LYP) 6–31 + G (d,p)/SMD basic set.

3.3.2. Molecular docking analysis of HDAC ii pocket

Histone deacetylase (HDAC2) belongs to the hydrolase family and is a promising target for cancers. Over-activity of HDAC2 can lead to various forms of cancer such as breast cancer, as well as colon cancer and cervical carcinoma (Yelton and Ray, 2018; Eckschlager et al., 2017). In this work, the affinity parameters for the histone deacetylase (HDAC2) showed strong interactions with B (−6.00 kcal mol-1) binding energy. *N*-(4-hydroxylbenzoyl)-1,3-benzodioxole-5-carboxamide (B) formed hydrogen bonding interactions with HIS 183 and TYR 209 in the HDAC II enzyme. It shows hydrogen atom (18H) of hydroxyl group (OH) forms H-bonds with His 183 (18H-N_{HIS183},bond length = 2.55 Å) and TYR 209 (18H-O_{TYR209}). This protein substract was also stabilised by hydrophobic interactions formed by PHE 155 and LEU 276. Next, *N*-(2-(benzo[d] (Feng et al., 2018; Wang et al., 2018)di oxol-5-yl)ethyl)-4-hydroxybenzamide (C) formed carbon hydrogen bond with ASP 104 (C-19H···O_{ASP104}, bond length = 3.65 Å) in HDAC 2 active site. Ligand C may block the aspartate (ASP 104) which is converted to asparagine (ASN) in cancer cells. Asparagine (ASN) plays important role in suppressing apoptotic cancer cell death (Chiu et al., 2020). Other than that, C was also stabilized by PHE 210, PHE 155 and PRO 34. The binding energy of C in the active site HDAC is −6.9Kcal/mol.

Lastly, it was observed that *tert*-butyl 2-(4-carbamoylphe noxy)-2-methylpropanoate (F) ligand formed hydrogen bonding interactions with HIS183 (12O··· H_{HIS183}, bond length = 2. 94 Å) and GLY154 (14H···O, bond length = 2.31 Å) in the HDAC II pocket. The affinity parameters for the histone deacetylase (HDAC2) showed strong interactions with F (−6.00 kcal mol-1) binding energy. Ligand interaction diagram of B, C, and F with active site of HDAC II receptor are shown in Fig. 4. Ligand docking analysis and binding energy for B,C and F in HDAC II enzyme are given in Table 5.

3.3.3. Molecular docking analysis of endothelial growth factor receptor (EGFR) pocket

Over-expression and mutation of EGFR receptor cause a wide range of endothelial tumours such as breast cancer, as well as lung cancer and skin cancer (Tian et al., 2020; Martin-Fernandez et al., 2019; Eck and Hahn, 2012; Uribe and Gonzalez, 2011). In this study, *N*-(2-(1,3-benzodioxol-5-yl)eth yl)-1H-indole-2-carboxamide (D) formed hydrogen interactions with ASP 831 and THR 8611 in the EGFR receptor. It showed hydrogen atom of amine (N-39H) formed H-bond with ASP831 (N-39H…OOCAsp831, bond length = 2.58 Å). Molecular docking suggested binding energy of D in the active site of EGFR is 8.4Kcal/mol. Inhibitor targeted the EGFR receptor to activate the anti-proliferation effect and increased the cytotoxic effect. Ligand interaction diagram of D with active site of epidermal growth factor receptor (EGFR) is shown in Fig. 5. Table 6 shows the ligand docking analysis of epidermal growth factor receptor (EGFR) for D.

3.4. MTT cell viability assay studies

First and foremost, E showed great cytotoxic activity against MCF-7 cell lines with IC50 value 5 μg/mL. Then, compound D showed good cytotoxic activity against MCF-7 cell lines with IC50 = 23 μg/mL, due to the presence of indole moiety. Apart from that, A, C, and F compounds showed moderate anti-proliferative effect against MCF-7 cell lines with IC50 value 37.5 μg/mL, 44 μg/mL, and 93 μg/mL respectively. Unfortunately, there was no 50% inhibition of MCF-7 cell growth occurring when treated with compounds B, G and H at any concentrations. The IC50 value decreased as follows: F(93 μg/mL) > C(44 μg/mL) > A(37.5 μg/mL) > D(23 μg/mL) > E(5 μg/mL). The order of cytotoxic activity increase conformed with the decreases in IC50 values. The cytotoxicity of synthesized compounds against MCF7 is shown in Fig. 6.

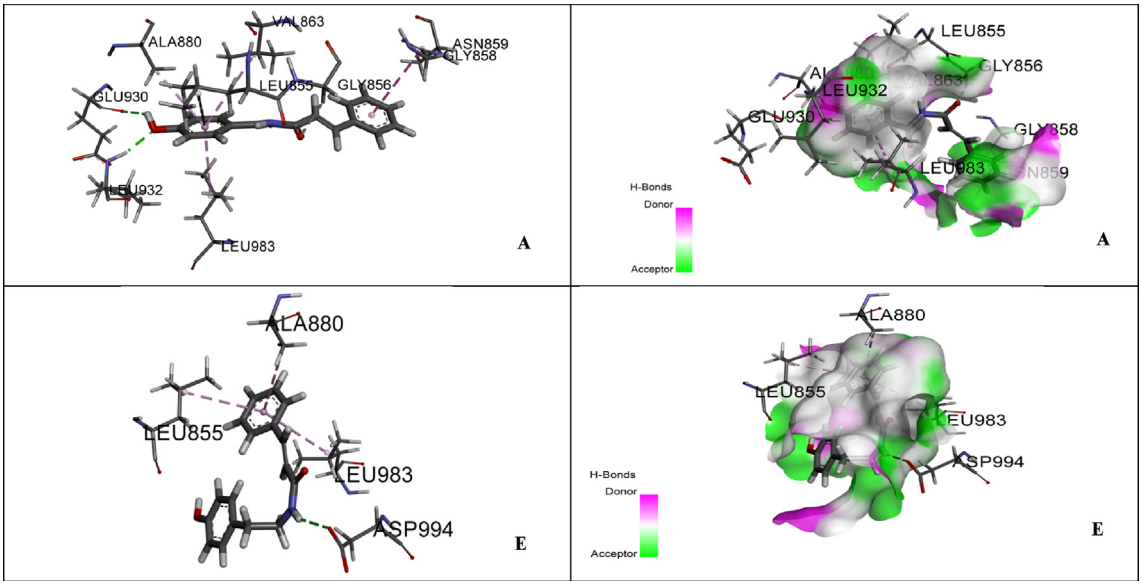

Fig. 3 Ligand interaction diagram of A and with active site of Janus kinase (II).

Table 4 0: Flexible ligand docking analysis of Janus Kinase II enzymes for compound A and E

Ligand	Key amino acid	Interaction	Bond length (Å)	Binding mode	Root mean square deviation (RMSD)	Bind energy (kcal/mol)
A	GLU 930	Hydrogen bond	2.32	6	1.185	−7.7
	LEU 932	Hydrogen bond	2.03			
	GLY 856	Carbon Hydrogen bond	2.47			
	ALA 880	hydrophobic	4.21			
	VAL 863	hydrophobic	4.83			
	GLY 858-ASN 859	hydrophobic	4.64			
		hydrophobic				
	LEU 855	hydrophobic	5.44			
	LEU 983	hydrophobic	4.30			
E	ASP 994	Hydrogen bond	2.37	6	2.001	−7.2
	LEU 983	hydrophobic	4.51			
	LEU 855	hydrophobic	4.45			
	ALA 880	hydrophobic	4.80			

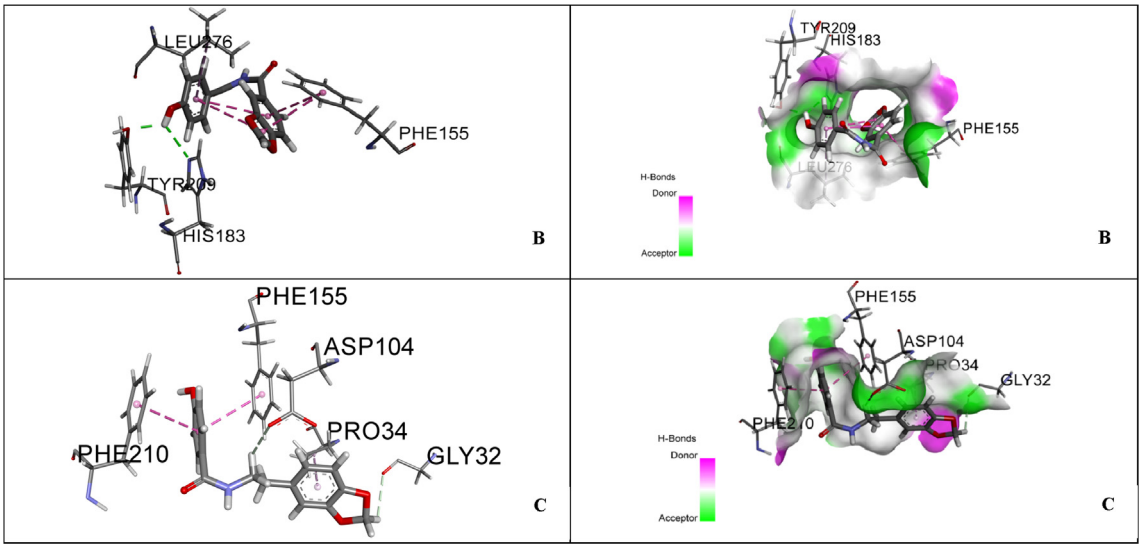

Fig. 4 Ligand interaction diagram of B,C, and F with active site of HDAC II receptor.

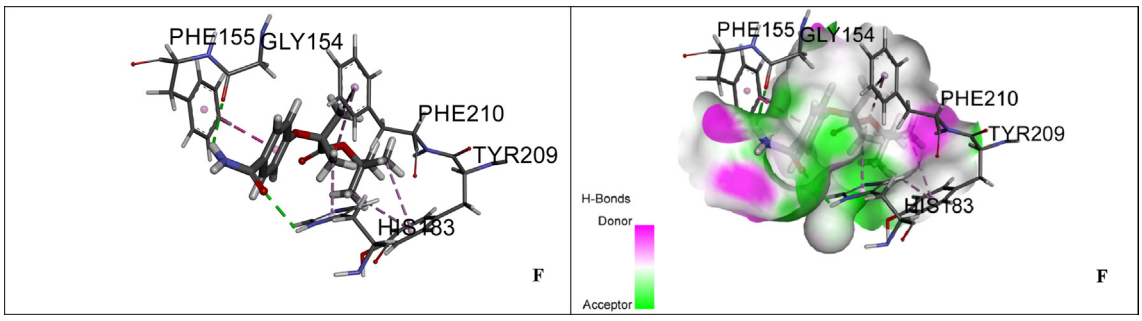

Fig. 4 (*continued*)

Table 5 0: Flexible ligand docking and binding energy for B,C and F in HDAC II enzyme

Ligand	Key amino acid	Interaction	Bond length (Å)	Binding mode	Root mean square deviation (RMSD)	Bind energy Kcal/mol
B	HIS 183	Hydrogen bond	2.55	2	1.837	−6.00
	TYR 209	Hydrogen bond	1.99			
	LEU 276	Hydrophobic	4.98			
	PHE 155	Hydrophobic	4.01,4.35			
	LEU 276	Hydrophobic	4.98			
C	ASP 104	Carbon Hydrogen bond	2.99	2	1.003	−6.90
	GLY 32	Carbon Hydrogen bond	2.98			
	PHE 210	Hydrophobic	4.39			
	PHE 155	Hydrophobic	4.21			
	PRO 34	Hydrophobic	4.05			
F	HIS 183	Hydrogen bond	2.41	4	1.063	−6.00
	GLY 154	Hydrogen bond	2.31			
	PHE210-	Hydrophobic	4.76			
	TYR 209	Hydrophobic	5.37			
	PHE 155	Hydrophobic	4.00			

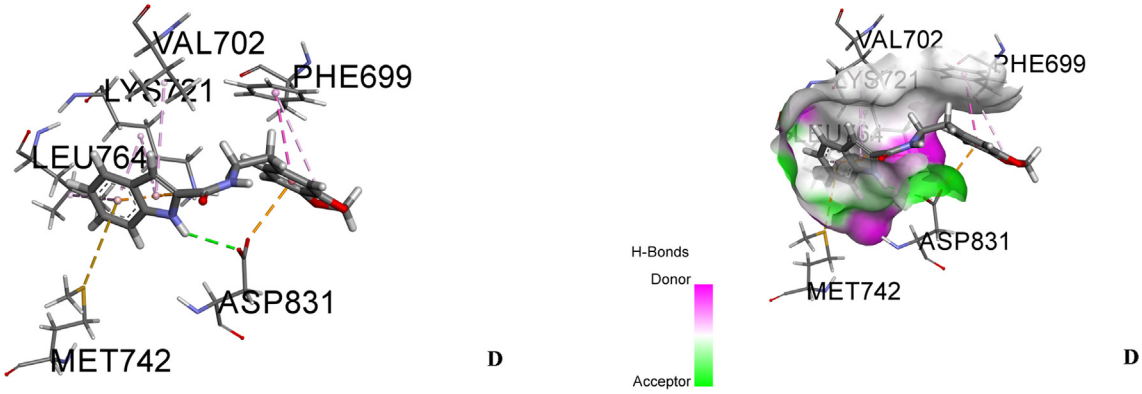

Fig. 5 Ligand interaction diagram of D with active site of epidermal growth factor receptor (EGFR).

Table 6 Flexible ligand docking analysis of epidermal growth factor receptor (EGFR) for D

Ligand	Key amino acid	Interaction	Bond length (Å)	Binding mode	Root mean square deviation (RMSD)	Bind energy (kcal/mol)
D	ASP 831	Hydrogen bond	2.58	2	0.947	−8.4
	PHE 699	Hydrophobic	5.38			
	VAL 702	Hydrophobic	5.08			
	MET 742	Pi-sulphur	4.88			
	LEU 764	Hydrophobic	5.48			
	LYS721	Hydrophobic	4.35			

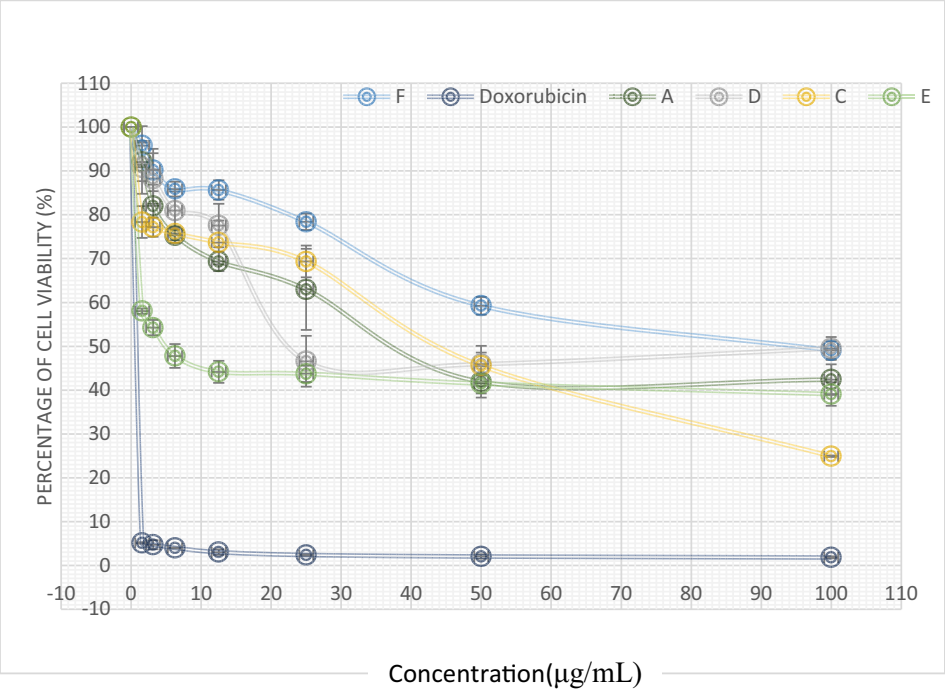

Fig. 6 Percentage of cell viability of MCF-7against different doses of compounds. Each value represents the mean ± SD from three separate experiments.

Table 7 IC50 values (μg/mL) of 4-hydroxbenzamide analogous after 72 h treatment and doxorubicin and valproic acid as reference compounds.

Ligand	Cell lines/ IC_{50} (μg/mL)		
	MCF 7	MDM-MD-231	NIH/3T3
A	37.5	35	34
B	*	33	*
C	44	41	*
D	23	*	*
E	5	5	*
F	93	47	*
G	*	*	*
H	*	*	*
I	N.d	N.d	N.d
J	N.d	N.d	N.d
k	N.d	N.d	N.d
Doxorubicin	1.00	1.00	4.00
Valproic acid [d]	465	267	N.d

Note: d = (Nafi et al., 2016).
* = No IC_{50} value.
N.d: not determined.

Besides, E showed great cytotoxicity against MDM-MD-231 cell lines with IC50 value 5 μg/mL. Apart from that, molecule A, B, C, and F showed moderate anti-proliferative effect against MDM-MD-231 cell lines with IC50 values 35 μg/mL, 33 μg/mL, 41 μg/mL, and 47 μg/mL respectively. The valproic acid displayed 50% of MDM-MD-231cell growth at the high concentration of 267 μg/mL. Valproic acid is a weak HDAC inhibitor used for the treatment of breast cancer (MDM-MD-231) in phase 2 clinical (Wawruszak et al., 2015). The IC50 value decreased as follows: valproic acid (267 μg/mL) > F(47 μg/mL) > C(41 μg/mL) > A(35 μg/mL) > B(33 μg/mL) > E(5 μg/mL). The order of cytotoxic activity increase conformed with the decrease in IC50 values. IC_{50} of synthesized compounds are shown in Table 7. The cell viability of MDM-MD-231 is shown in Fig. 7.

We found that α, β-unsaturated carbonyl fragment (Compounds A and E) triggered the cytotoxic effect in MCF-7 cells line and MDM-MD-231. Compound E was more flexible than compound A in the JAK2 enzymes due to the presence of ethyl linkage. Compound F showed less cytotoxic effect in MCF-7 and MDM-MD-231 cell lines due to steric effect of *tert*-butyl ester fragment and less flexibility in HDAC2 enzymes upon ligand binding.

As shown in Fig. 8, 4-hydroxylbenzamide (B, C, D, E, F,) demonstrated less than 50% of cell growth inhibition at a concentration less than 100 μg/mL, which indicates that the studied compounds (B, C, D, E, F) were nontoxic towards 3 T3/NIH cell lines. The half-maximal inhibitions were only exhibited by compounds A at the highest concentration (34 μg/mL). Compound A showed less toxicity toward NIH/3T3 cell lines. In the present work, doxorubicin and valproic acid acted as standard drugs.

4. Conclusion

In this study, DFT calculations and molecular docking suggested that A, B, D and E may be considered as potential anti-cancer agents. They can be further examined in future

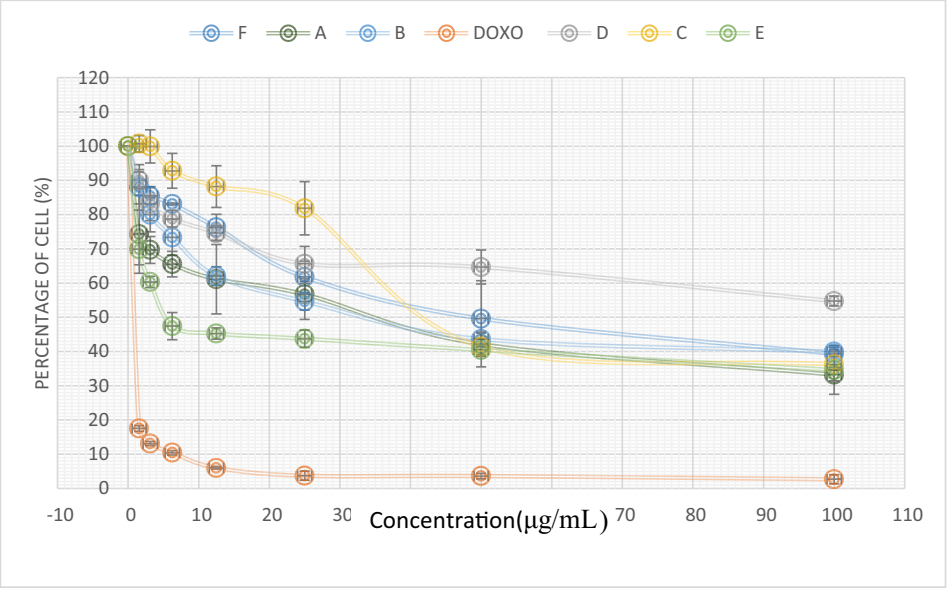

Fig. 7 Percentage of cell viability of MDA-MD-231 against different doses of compounds. Each value represents the mean ± SD from three separate experiments.

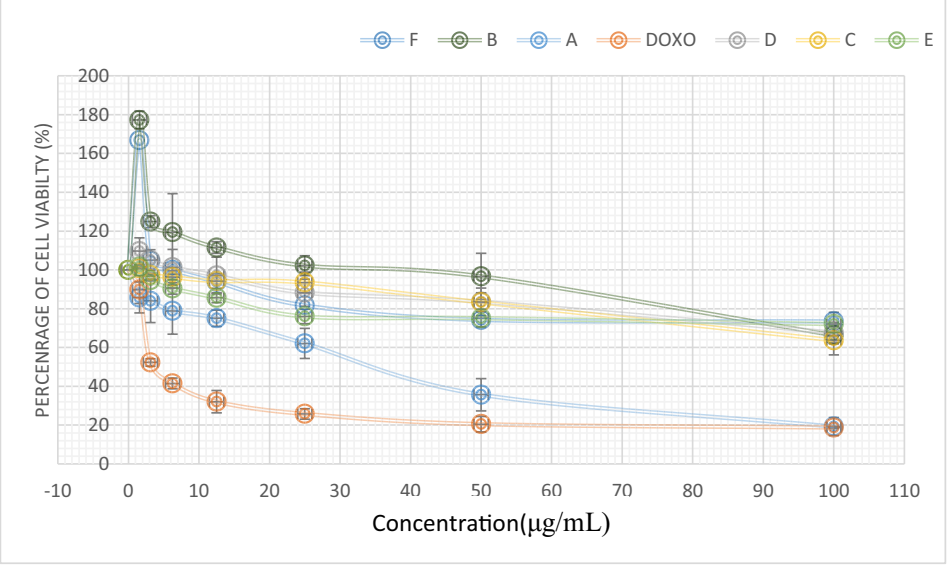

Fig. 8 Percentage of cell viability of NIH/3T3 against different doses compounds. Each value represents the mean ± SD from three separate experiments.

studies, such as studies combining them with DNA binding agent and studies of inhibitory assays. The molecular docking results showed that hydrogen bond interaction plays a crucial role in contributing to molecular interaction of active compound and targeted enzymes. In conclusion, all of these compounds did not show any cytotoxic effect on fibroblast (NIH/3T3) cell lines and the results certified that these compounds are potential anti-breast cancer agents. Molecule E was found to have significant apoptosis against MCF 7 cell line and MDM-MD-231 cell line with IC50 value 5.0 µg⁄mL and 5.0 µg⁄mL respectively.

Declaration of Competing Interest

The authors declare that they have no known competing financial interests or personal relationships that could have appeared to influence the work reported in this paper.

Acknowledgments

The authors wish to thank the Ministry of Higher Education (MOHE) Malaysia for financial funding through Trans Disciplinary Research Grant Scheme (TRGS: 59422, 2016-2019).

Appendix A. Supplementary material

Supplementary data to this article can be found online at https://doi.org/10.1016/j.arabjc.2021.103510.

References

Feng, Y., Spezia, M., Huang, S., Yuan, C., Zeng, Z., Zhang, L., Ji, X., Liu, W., Huang, B., Luo, W., Liu, B., 2018. Breast cancer development and progression: Risk factors, cancer stem cells, signaling pathways, genomics, and molecular pathogenesis. Genes Dis. 5 (2), 77–106.

Elkum, N., Al-Tweigeri, T., Ajarim, D., Al-Zahrani, A., Amer, S.M. B., Aboussekhra, A., 2014. Obesity is a significant risk factor for breast cancer in Arab women. BMC cancer 14 (1), 1–10.

Wang, C., Kar, S., Lai, X., Cai, W., Arfuso, F., Sethi, G., Kumar, A. P., 2018. Triple negative breast cancer in Asia: An insider's view. Cancer Treat. Rev. 62, 29–38. https://doi.org/10.1016/j.ctrv.2017.10.014.

Britschgi, A., Radimerski, T., Bentires-Alj, M., 2013. Targeting PI3K, HER2 and the IL-8/JAK2 axis in metastatic breast cancer: Which combination makes the whole greater than the sum of its parts? Drug Resist. Updates 16 (3–5), 68–72. https://doi.org/10.1016/j.drup.2013.10.001.

Singh, P. and Bast, F., 2014. In silico molecular docking study of natural compounds on wild and mutated epidermal growth factor receptor. *Medicinal Chemistry Research*, *23*(12), pp.5074-5085. http://DOI 10.1007/s00044-014-1090-1.

Lin, T.E., Huang Fu, W.C., Chao, M.W., Sung, T.Y., Chang, C.D., Chen, Y.Y., Hsieh, J.H., Tu, H.J., Huang, H.L., Pan, S.L., & Hsu, K.C. (2018). A novel selective JAK2 inhibitor identified using pharmacological interactions. *Frontiers in pharmacology*, *9*, 1-14. https://doi.org/10.3389/fphar.2018.01379.

Yelton, C.J., Ray, S.K., 2018. Histone deacetylase enzymes and selective histone deacetylase inhibitors for antitumor effects and enhancement of antitumor immunity in glioblastoma. Neuroimmunol. Neuroinflammat. 5 (11), 1–18. https://doi.org/10.20517/2347-8659.2018.58.

Jia, L.Y., Shanmugam, M.K., Sethi, G., Bishayee, A., 2016. Potential role of targeted therapies in the treatment of triple-negative breast cancer. Anticancer Drugs 27 (3), 147–155. https://doi.org/10.21873/anticanres.13722.

Tian, M., Qi, Y., Zhang, X., Wu, Z., Chen, J., Chen, F., Zhang, S., 2020. Regulation of the JAK2-STAT5 pathway by signaling molecules in the mammary gland. Front. Cell Dev. Biol. 8, 1382. https://doi.org/10.3389/fcell.2020.604896.

Siegelin, M.D., Borczuk, A.C., 2014. Epidermal growth factor receptor mutations in lung adenocarcinoma. Lab. Invest. 94 (2), 129–137.

Nikolic, V., Savic, I., Savic, I., Nikolic, L., Stankovic, M., Marinkovic, V., 2011. Paclitaxel as an anticancer agent: isolation, activity, synthesis and stability. Open Med. 6 (5), 527–536. https://doi.org/10.2478/s11536-011-0074-5.

Staels, B., Fruchart, J.C., 2005. Therapeutic roles of peroxisome proliferator–activated receptor agonists. Diabetes 54 (8), 2460–2470. https://doi.org/10.2337/diabetes.54.8.2460.

Stec, J., Huang, Q., Pieroni, M., Kaiser, M., Fomovska, A., Mui, E., Witola, W.H., Bettis, S., McLeod, R., Brun, R., Kozikowski, A.P., 2012. Synthesis, biological evaluation, and structure–activity relationships of N-benzoyl-2-hydroxybenzamides as agents active against P. falciparum (K1 strain), trypanosomes, and leishmania. J. Med. Chem. 55 (7), 3088–3100. https://doi.org/10.1021/jm2015183.

Liew, K.M., Tagg, T., Khairul, W.M., 2019. Synthesis and characterisation of N-analineferrocenylamide via carbodiimide coupling. Malaysian J. Analyt. Sci. 23 (2), 189–196. https://doi.org/10.17576/mjas-2019-2302-02.

Ediriweera, M.K., Tennekoon, K.H. and Samarakoon, S.R. 2019. Emerging role of histone deacetylase inhibitors as anti-breast-cancer agents. *Drug discovery today*, *24*(3), pp.685-702. https://DOI: 10.1016/j.drudis.2019.02.003.

Abu Bakar, A., Akhtar, M.N., Mohd Ali, N., Yeap, S.K., Quah, C.K., Loh, W.S., Alitheen, N.B., Zareen, S., Ul-Haq, Z., Shah, S.A.A., 2018. Design, synthesis and docking studies of flavokawain B type chalcones and their cytotoxic effects on MCF-7 and MDA-MB-231 cell lines. Molecules 23 (3). https://doi.org/10.3390/molecules23030616.

Kumar, N., Tomar, R., Pandey, A., Tomar, V., Singh, V.K. and Chandra, R. 2018. Preclinical evaluation and molecular docking of 1, 3-benzodioxole propargyl ether derivatives as novel inhibitor for combating the histone deacetylase enzyme in cancer. *Artificial cells, nanomedicine, and biotechnology*, *46*(6), pp.1288-1299. https://DOI: 10.1007/s40203-020-00057-8.

Piekna-Przybylska, D., Bambara, R.A. and Balakrishnan, L. 2016. Acetylation regulates DNA repair mechanisms in human cells. *Cell Cycle*, *15*(11), pp.1506-1517.https://DOI: 10.1080/15384101.2016.1176815.

Eckschlager, T., Plch, J., Stiborova, M. and Hrabeta, J. 2017. Histone deacetylase inhibitors as anticancer drugs. *International journal of molecular sciences*, *18*(7), pp.1-25. https://doi: 10.3390/ijms18071414.

Ur Rashid, H., Xu, Y., Ahmad, N., Muhammad, Y., Wang, L., 2019. Promising anti-inflammatory effects of chalcones via inhibition of cyclooxygenase, prostaglandin E2, inducible NO synthase and nuclear factor κb activities. Bioorg. Chem. 87, 335–365. https://doi.org/10.1016/j.bioorg.2019.03.033.

Gonring-Salarini, K. L., Conti, R., Andrade, J. P. D., Borges, B. J. P., Aguiar, A. C. C., Souza, J. O. D., Zanini, C. L., Oliva, G., Tenorio, J.C., Ellena, J, Bastida, J., Guido, R,V,C., & Borges, W. D. S. (2019). In vitro antiplasmodial activities of alkaloids isolated from roots of Worsleya procera (Lem.) Traub (Amaryllidaceae). *Journal of the Brazilian Chemical Society*, *30*(8), pp. 1624-1633. https://doi.org/10.21577/0103-5053.20190061.

Szczepańska, K., Karcz, T., Mogilski, S., Siwek, A., Kuder, K.J., Latacz, G., Kubacka, M., Hagenow, S., Lubelska, A., Olejarz, A., Kotańska, M., 2018. Synthesis and biological activity of novel tert-butyl and tert-pentylphenoxyalkyl piperazine derivatives as histamine H3R ligands. Eur. J. Med. Chem. 152, 223–234. https://doi.org/10.1016/j.ejmech.2018.04.043.

Foresman, J., Frisch, A., 1996. Exploring Chemistry with Electronic Structure Methods. Gaussian Inc, Pittsburgh, PA.

Lewars, E., 2003. Computational Chemistry - Introduction to the Theory and Applications of Molecular and Quantum Mechanics. Kluwer Academic Publishers, Dordrecht.

Parr, R., Pearson, R., 1983. Absolute hardness: companion parameter to absolute electronegativity. J. Am. Chem. Soc. 105, 7512–7516.

Parr, R., Yang, W., 1984. Density functional approach to the frontier-electron theory of chemical reactivity. J. Am. Chem. Soc. 106, 4049–4050.

Parr, R., Szentpaly, L., Liu, S., 1999. Electrophilicity index. J. Am. Chem. Soc. 121, 1922–1924.

Kaur, K., Kaur, P., Mittal, A., Nayak, S.K., Khatik, G.L., 2017. Design and molecular docking studies of novel antimicrobial peptides using Autodock molecular docking software. Asian J. Pharm. Clin. Res. 10, 28–31. https://doi.org/10.22159/ajpcr.2017.v10s4.21332.

www.rcsb.org.pdb (Accessed 1 December 2020).

Nafi, N.E.M., Zin, N.B.M., Pauzi, N., Khadar, A.S.A., Anisava, A.R., Badiazaman, A.A.M., Mohd, K.S., 2016. Cytotoxicity, antioxidant and phytochemical screening of propolis extracts from four different Malaysian stingless bee species. Malaysian J. Fundamental Appl. Sci., 307–312 https://doi.org/10.11113/mjfas.v15n2-1.1542.

Rocha, J.A., Rego, N.C., Carvalho, B.T., Silva, F.I., Sousa, J.A., Ramos, R.M., Lima, F.C., 2018. Computational quantum chemistry, molecular docking, and ADMET predictions of imidazole

alkaloids of Pilocarpus microphyllus with schistosomicidal properties. PLoS ONE 13, (6). https://doi.org/10.1371/journal.pone.0198476 e0198476.

Jordaan, M.A., Ebenezer, O., Damoyi, N. and Shapi, M. 2020. Virtual screening, molecular docking studies and DFT calculations of FDA approved compounds similar to the non-nucleoside reverse transcriptase inhibitor (NNRTI) efavirenz. *Heliyon*, *6*(8), pp.1-11. https://doi: 10.1016/j.heliyon.2020.e04642.

Chiu, M., Taurino, G., Bianchi, M.G., Kilberg, M.S., Bussolati, O., 2020. Asparagine Synthetase in Cancer: Beyond Acute Lymphoblastic Leukemia. Front. Oncol. 9, 1–10. https://doi.org/10.3389/fonc.2019.01480.

Eck, M.J., Hahn, W.C., 2012. EGFR in Limbo. Cell 149 (4), 735–737. https://doi.org/10.1016/j.cell.2012.04.015.

Martin-Fernandez, M.L., Clarke, D.T., Roberts, S.K., Zanetti-Domingues, L.C., Gervasio, F.L., 2019. Structure and dynamics of the EGF receptor as revealed by experiments and simulations and its relevance to non-small cell lung cancer. Cells 8 (4), 1–33. https://doi.org/10.3390/cells8040316.

Uribe, P., Gonzalez, S., 2011. Epidermal growth factor receptor (EGFR) and squamous cell carcinoma of the skin: molecular bases for EGFR-targeted therapy. Pathology-Res. Pract. 207 (6), 337–342. https://doi.org/10.1016/j.prp.2011.03.002.

Wawruszak, A., Luszczki, J.J., Grabarska, A., Gumbarewicz, E., Dmoszynska-Graniczka, M., Polberg, K. and Stepulak, A., 2015. Assessment of interactions between cisplatin and two histone deacetylase inhibitors in MCF-7, T47D and MDA-MD-231 human breast cancer cell lines–an isobolographic analysis. *PLoS One*, *10* (11), pp.1-19. https://DOI: 10.1371/journal.pone.0143013.